

Measuring Near-Surface Firn Structure in the Percolation Zone of the Greenland Ice Sheet using Ground-Penetrating Radar

Diploma thesis

Department of Geosciences at the
University of Bremen

in cooperation with the
Alfred Wegener Institute for Polar and Marine Research

submitted by Thorben Dunse

May 22, 2006

Abstract

Contents

Abstract	III
List of Figures	VII
List of Tables	VIII
1. Introduction	1
1.1. Radio-echo sounding of snow & ice	1
1.2. CryoSat land-ice validation	3
1.3. Area of investigation	6
2. Theory of Electromagnetic Wave Propagation in Snow and Firn	9
2.1. Governing equations	9
2.2. The dielectric properties of snow and firn	11
2.3. Propagation of electromagnetic waves in snow and firn	15
2.4. Ground-penetrating radar (GPR)	18
3. Field Experiment at the EGIG-Line	21
3.1. Snow pits and firn cores	22
3.2. GPR measurements	24
3.3. Differential global-positioning system (DGPS)	29
4. GPR Processing	32
4.1. Correction of time of first arrival	34
4.2. Frequency filtering	36
4.3. Moving average filtering	36

4.4. Complex trace analysis	37
4.5. Final smoothing	38
4.6. Automatic gain	38
4.7. Data output	39
4.8. Interpretation	39
5. Results	44
5.1. GPR-data properties	44
5.2. Surface topography	46
5.3. Internal reflection horizons	47
6. Discussion & Conclusions	52
6.1. Frequency dependency of results	52
6.2. Local-scale spatial variability in snow accumulation	54
6.3. Large-scale spatial distribution of snow	57
6.4. Radar measurements versus firn-core records	59
6.5. Accumulation rate estimates	61
Acknowledgements	69
A. Scripts & routines	70
B. Data	72
B.1. GPR	72
B.2. GPS	72
B.3. Snow-stratigraphy	72
C. Results	74
C.1. 100 by 100-m grid	74
C.2. 1 by 1-km square	80
D. Erklärung	86

List of Figures

1.1. Cryosat from an artist's view	3
1.2. Map of survey area	5
1.3. Ground-based activities during CryoVex 2004	5
1.4. Snow facies in the accumulation area	7
1.5. Snow zones of the Greenland Ice Sheet	7
2.1. Permittivity-density relation and resulting EM-wave speed	14
2.2. Snell's law	16
3.1. Location of radar profiles	21
3.2. Density-depth, velocity-depth and accumulation-depth models	23
3.3. GPR-equipment	25
3.4. Estimated maximum error in IRH-depth computation	28
3.5. Correction of GPS coordinates	30
3.6. GPS tracks and ideal grid-points	31
4.1. Sketch of DISCO-processing flow for radar data.	33
4.2. Effect of static correction	34
4.3. Individual correction of first-arrival times	35
4.4. Effect of frequency filtering	36
4.5. Effect of displaying envelope instead of amplitude	37
4.6. Effect of automatic gain	38
4.7. Radar section with amplitude displayed	40
4.8. Radar section with envelope displayed	41
5.1. Arbitrary 500-MHz profile–amplitude, envelope, digitized horizons	45

5.2. Surface-elevation model	47
5.3. Internal reflection horizons (IRH)	48
5.4. Contour plots of selected IRH	49
5.5. Histograms of IRH-depths and bandwidths	50
5.6. Systematic IRH-inclination over 1 by 1-km ² square	51
6.1. Comparison of antenna frequencies - depth	53
6.2. Comparison of antenna frequencies - bandwidth	54
6.3. Contour plots of normalized IRH-depths	57
6.4. Spatial variability along 1-km sections	58
6.5. Radar measurement versus firn-core record	60
B.1. Shallow density-depth profiles	73
C.1. Histograms of IRH-depths and bandwidths	79

List of Tables

2.1. Electrical properties of common earth surface materials	12
2.2. EM-wave velocities in ice	15
2.3. GPR frequencies and corresponding resolution	19
3.1. GPR survey-parameters	25
3.2. Estimated maximum error in IRH-depth computation	28
6.1. Internal reflection horizons and their spatial variability	55
6.2. Depth, mass and accumulation-rate estimates for internal horizons	62
C.1. Mean values of TWT - grid	75
C.2. Mean values of depth - grid	76
C.3. Mean values of cumulative mass - grid	77
C.4. Comparison of antenna frequencies	78
C.5. Mean values of TWT - 1 by 1-km square	81
C.6. Mean values of depth - 1 by 1-km square	82
C.7. Mean values of cumulative mass - 1 by 1-km square	83
C.8. Spatial variability in accumulation - 1 by 1-km square	84

1. Introduction

In spring 2004 the Alfred Wegener Institute for Polar and Marine Research (AWI) performed ground-based, local-scale radar measurements in the western part of the Greenland Ice Sheet. The survey area was located at the lower end of the EGIG-line – named after the *Expédition Glaciologique Internationale au Groenland* (EGIG; 1957-60 and 1964-68), and spanning across the ice sheet from West (70 °N, 48 °W) to East (72 °N, 29 °W). The fieldwork was a contribution to CryoVex2004, one of CryoSat’s validation campaigns. Near-surface ice layers interact with CryoSat’s radar altimeter and complicate interpretation of it’s record. To identify internal reflection horizons in the radar-record and to investigate their spatial variation is part of the ground-truthing. Furthermore, these information help to investigate the representativeness of point measurements, such as from firn cores and snow pits.

This introduction gives an overview of many-fold applications of radar systems in the field of glaciology. It outlines the objective of the present study and provides background information on the survey area. The theory of electromagnetic wave propagation is the basement for any radar survey and will be discussed in chapter 2, preceding a description of the field experiment and collected data sets (chapter 3). The extensive processing of the radar data will be addressed in chapter 4, before final presentation of the results and their discussion in chapter 5 to 7.

1.1. Radio-echo sounding of snow & ice

Ground-penetrating radar (GPR), also referred to as radio-echo sounding (RES) has become a standard tool in the field of glaciology since the early 1960’s. First indications of the relative transparency of snow and ice to electromagnetic waves in the VHF and UHF bands (~ 10 MHz to 1 GHz) was given by pilots, repeatedly reporting malfunctioning of radar altimeters over large ice masses (Waite and Schmidt, 1961). RES is an active remote-sensing technique. An electromagnetic

1. Introduction

signal is emitted from a transmitting antenna and penetrates the ice. Part of the signal is reflected at inhomogeneities within the ice or the underlying bedrock and detected with a receiving antenna. The signal's amplitude is measured as a function of two-way traveltime, the time needed for the signal to travel from the antennae to the reflecting object and back. Traveltime can be converted to depth, if the velocity of propagation throughout the firn and ice is known. Abrupt changes of the complex dielectric constant are the source of reflections. While changes in the conductivity, like acidic layers of volcanic origin, dominate reflections from deeper parts of an ice sheet, permittivity changes, strongly related to density, are most important for shallow return echoes ($\lesssim 200$ m). RES has been extensively used both from ground-based and airborne platforms, to measure the thickness of glaciers, ice sheets and shelves (Evans, 1963; Walford, 1964) and to map the topography of the underlying bedrock. The information is an important input parameter for numerical ice sheet models, e.g. flow models or for the optimum location of deep-drill sites, in order to retrieve an ice-core climate record with minimum distortion (Steinhage, 2001). Knowing the absolute position of the instrument, airborne RES-range measurements produce surface-elevation models as a by-product, but are commonly derived by satellite radar or laser altimetry (Bamber *et al.*, 2004). Reflections from deep englacial layers, believed to represent time-markers, so-called isochrones, enable the calibration of age-depth scales between a few deep cores, and supply important information on ice-sheet layering and hence past accumulation rates (Jacobel and Hodge, 1995; Baldwin *et al.*, 2003). Near-surface investigations deploying higher-frequency systems ($\gtrsim 500$ MHz) aim at the physical firn structure (Zabel *et al.*, 1995) and on the spatial and temporal variability in snow accumulation (Kohler *et al.*, 1997; Richardson *et al.*, 1997; Richardson-Näslund and Holmlund, 1999). A major advantage of radar soundings compared to conventional methods in determining recent mass balance rates, e.g. snow-pit, firn-core and stake measurements, is the possibility to obtain continuous profiles from moving platforms in high spatial resolution. This helps to quantify the representativeness of point measurements and to put them in a larger spatial context. Furthermore, radar measurements have been used to identify englacial and subglacial structures, including crevasses and lakes (Oswald and Robin, 1973; Siegert *et al.*, 1996), to study the conditions at the ice-bed interface (Oswald, 1975) and to identify fast flowing ice streams as regions of intense shear (Bindschadler, 1984). In addition, signal absorption and fading

patterns provided information on the thermal structure and liquid water content of ice masses (Pettersen *et al.*, 2003; Björnson *et al.*, 1996).

1.2. CryoSat land-ice validation

The present study is a contribution to the validation and calibration experiments of the CryoSat satellite radar altimetry mission (Figure 1.1). On October 8, 2005, the CryoSat mission failed due to a failure in the launching sequence. However, in February 2006, the member states of the European Space Agency (ESA) agreed on building and launching a CryoSat recovery mission, CryoSat-2, expected to be launched in March 2009 (ESA-website, 2006). The objective of CryoSat is to monitor changes in the elevation and thickness of polar ice sheets and floating sea ice over a period of three years.

CryoSat is equipped with an interferometric radar altimeter (SIRAL), designed to be able to detect even irregular sloping edges of land ice, as well as non-homogenous sea ice, from an altitude of 700 km. The accurate position of the spacecraft will be determined with an onboard ranging instrument called a Doppler Orbitography and Radiopositioning Integrated by Satellite (DORIS) receiver supplemented by a laser retro-reflector system. The signal return time will reveal the surface elevation. Providing a unique data set over large and remote areas at regular time-intervals,

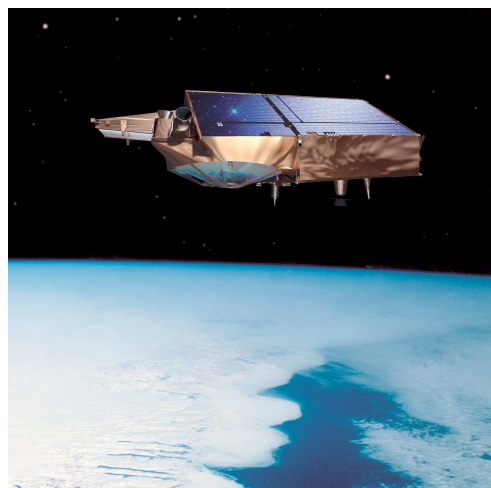


Figure 1.1.: Cryosat from an artist's view. (Taken from the ESA's Living Planet Programme-website (2006)).

1. Introduction

CryoSat shall identify regions and periods of mass accumulation and mass loss and further contribute to the question of whether global climate change is causing the polar ice caps to shrink. The accuracy to which satellite-measured surface elevation changes represent a change in ice mass is associated with two major problems:

- the accuracy to which satellite-derived surface elevation represent actual surface elevation, and
- the extend to which changes in actual surface-elevation represent mass change.

Principal objective of all CryoSat land ice validation activities is to assess and quantify the uncertainty in the CryoSat measurements and to investigate the interaction of the Ku-band radar altimeter (center frequency of approx. 13.5 GHz) with the upper meters of the snowpack. The great variety of naturally occurring snow and ice surfaces makes this a complex task, because the radar response highly depends on the physical properties of the snowpack.

During CryoVex2004 AWI performed ground-based radar measurements of the firn structure using 500 and 800 MHz antenna frequencies. The GPR-profiles form a detailed 100 by 100-meter grid and a 1 by 1-kilometer square, located at point T05 of the EGIG-line (70 °N, 47 °W; Figure 1.2). The altitude of around 1940 meter above sea level is located within the percolation zone. Major aim was to identify internal reflection horizons and to investigate their spatial variation on a scale of 100 to 1000 m. Results from the ground-based measurements enhance the understanding of airborne records (ground-truthing), also retrieved during CryoVex2004, using the Airborne Synthetic Aperture and Interferometric Radar Altimeter System (ASIRAS), deployed on a Polar 2 aircraft, type Dornier 228. ASIRAS resembles SIRAL, CryoSat's radar altimeter, allowing direct comparison of the records. Processing and Interpretation of airborne records from T05 are subject of a PhD-study within the section of glaciology at the AWI (by Veit Helm). The ground-based radar measurements were supplemented with simultaneous positioning measurements, derived from Differential Global Positioning System (DGPS) and stratigraphic records from snow pits and firn cores. These information, supplied from the Institute of Geography at the University of Edinburgh, form the basis for the conversion of traveltime to depth.

1.2. CryoSat land-ice validation

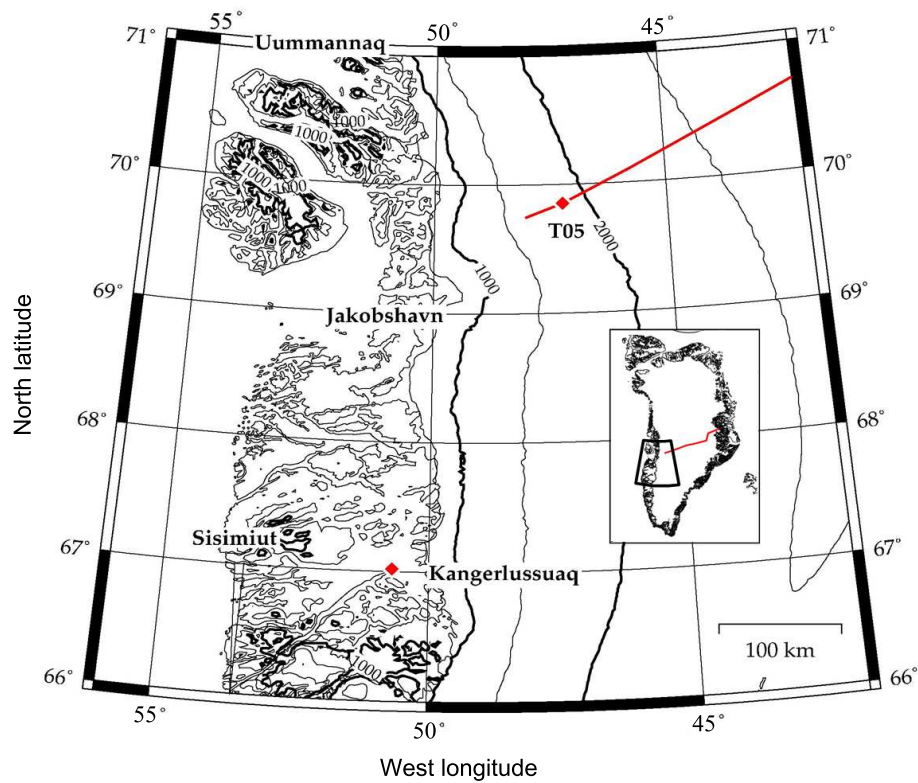


Figure 1.2.: Map of the survey area around point T05 at the western flank of the Greenland Ice Sheet. The line across the ice sheet indicates the position of the EGIG-line.



Figure 1.3.: Ground-based activities during CryoVex 2004. (A) The man-pulled sledge hosting GPR and GPS-systems. (B) Retrieval of a shallow firn-core for physical properties measurements.

1. Introduction

1.3. Area of investigation

The Greenland Ice Sheet covers an area of 1.7×10^6 km² and contains a volume of 2.82×10^6 km³ of ice, only outnumbered in size by the Antarctic Ice Sheet (13.6×10^6 km², $\sim 30 \times 10^6$ km³; Dowdeswell and Evans (2004)). While the response of the Antarctic Ice Sheet to global warming is very uncertain – it might grow due to increased precipitation and if sufficiently cold temperatures are sustained – there are indications that the Greenland Ice Sheet is actually thinning. Recent airborne laser altimetry suggests that the ice sheet is in balance on average above an altitude of 2000 m but experiences peripheral thinning at lower elevations, with rates exceeding 1 m a^{-1} close to the coast (Krabill *et al.*, 2000). If it were about to melt completely, it would raise global sea level by about 6 m (Letréguilly *et al.*, 1991). Krabill *et al.* (2000) estimated the mass net loss for the last decade to be about 51 km³ corresponding to a sea-level rise of 0.13 mm per year or 7 % of the observed global rise. The largest contribution is currently from mountain glaciers outside the polar regions, rapidly melting under current climate conditions, but only accounting for about 3 % of global ice mass (Arendt *et al.*, 2002).

The physical properties of snow and firn on the Greenland Ice Sheet are controlled by the spatial variation in summer melt. Close to the coast, summer melting completely removes the seasonal snow cover and exposes bare, often highly crevassed ice. This margin forms the ablation zone, where the ice sheet experiences net-mass loss. At slightly higher elevations follows the wet-snow or soaked zone. This zone is already part of the accumulation area, where mass is added to the ice sheet, as seen in Figure 1.4. Here, summer temperatures are sufficient to raise the whole previous winter's snow-pack temperature to melting point and saturate it with meltwater (Paterson, 1994). Large part of the Greenland Ice Sheet are occupied by the percolation zone (Figure 1.5). In the percolation zone, snow metamorphism is highly influenced by seasonal melting and refreezing. During the summer months, surface meltwater percolates downwards through the previous winter's snowpack. The snow is cold (below melting point) and restricts meltwater flow, so that it refreezes and forms massive ice layers, lenses and pipes, causing a marked contrast in the vertical structure of winter and summer firn (Jezek *et al.*, 1994). Freezing of one gram of water releases latent heat and provides enough energy to raise the temperature of 160 grams of snow by 1°C (Paterson, 1994). Refreezing of meltwater is therefore

1.3. Area of investigation

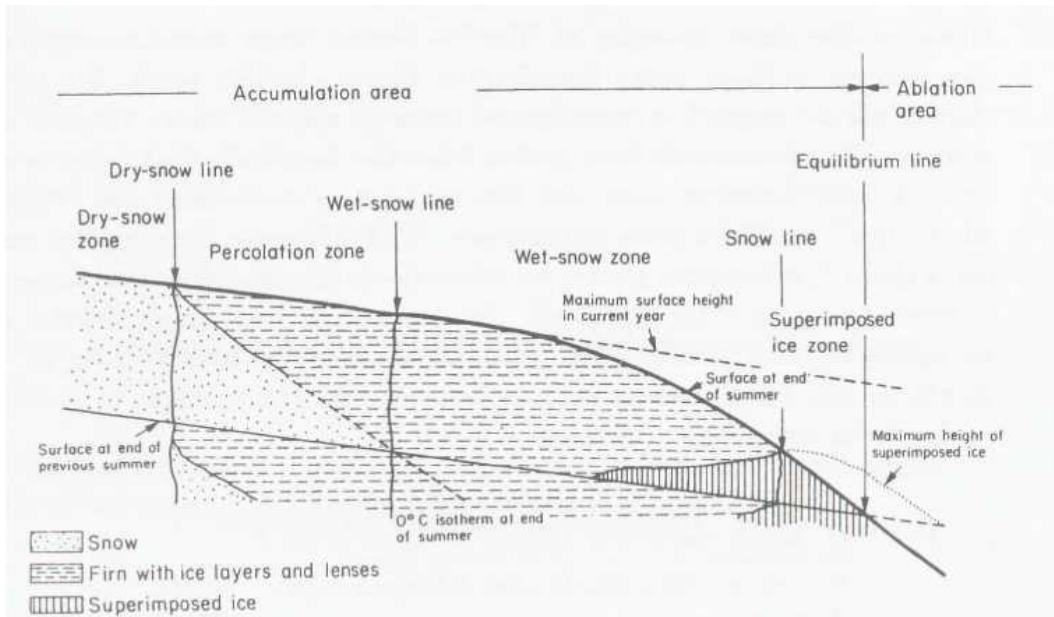


Figure 1.4.: Snow facies in the accumulation area. (Taken from Paterson (1994).)

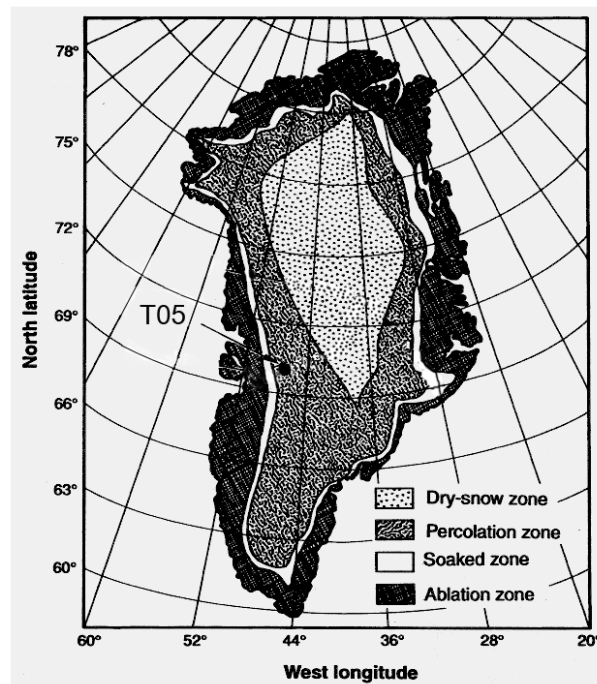


Figure 1.5.: Map of Greenland showing the different snow zones defined by Benson (1962), and the location of point T05 of the EGIG-line. (Modified from Rignot *et al.* (1993).)

1. Introduction

the most important factor in warming the snow. Higher temperatures enhance snow metamorphism. The central part of the Greenland Ice Sheet stays below freezing temperatures the whole year round. Melting barely occurs here, even in summer, so it is called the dry-snow zone. The ice structures in the percolation facies have been known for producing very high radar backscatter (Jezek *et al.*, 1994). Ice structures also form in the wet-snow zone, but saturation with liquid water highly attenuates the radar signal and obstacles only yield weak return echoes. The cold and dry snow in central parts of the Greenland Ice Sheet is very transparent to electromagnetic waves and allows deep penetration, but solid-ice structures are absent.

2. Theory of Electromagnetic Wave Propagation in Snow and Firn

The theory of electromagnetic waves in snow and ice and its implications for the application of radar-echo sounding in the field of glaciology has been thoroughly discussed by Bogorodsky *et al.* (1985); Hempel (1994); Dowdeswell and Evans (2004), and others. The discussions build-up on studies of the dielectric properties of snow and ice, which control the velocity and ray path geometry of a propagating electromagnetic signal (Looyenga, 1965; Glen and Paren, 1975; Robin, 1975; Kovacs *et al.*, 1995).

2.1. Governing equations

The propagation of an electromagnetic wave can be described by the wave equation which represents a solution of the Maxwell equations. These time-dependent equations form the basis in describing the relations between electric and magnetic fields. For a three-dimensional region in space without electric and magnetic current sources, but with properties to respond to electric and magnetic field energy, the equations can be written as:

$$\nabla \times \vec{H} = \frac{\partial \vec{D}}{\partial t} + \sigma \vec{E} = \varepsilon^* \frac{\partial \vec{E}}{\partial t} + \sigma \vec{E} \quad (\text{Ampere's Law}), \quad (2.1)$$

$$\nabla \times \vec{E} = -\mu^* \frac{\partial \vec{H}}{\partial t} = \frac{\partial \vec{B}}{\partial t} \quad (\text{Faraday's Law}), \quad (2.2)$$

$$\nabla \cdot \vec{B} = 0 \quad (\text{Gauss's Law for the magnetic field}), \quad (2.3)$$

2. Theory of Electromagnetic Wave Propagation in Snow and Firn

$$\nabla \cdot \vec{E} = 0 \quad (\text{Gauss's Law for the electric field}). \quad (2.4)$$

Here, \vec{H} is the magnetic field vector, \vec{B} is the magnetic flux density, \vec{E} is the electric field vector, and \vec{D} is the electric flux density. $\nabla \equiv \sum_{j=1}^3 \left(\frac{\partial}{\partial x_j} \vec{e}_{x_j} \right)$ is the Nabla-operator in cartesian coordinates and \vec{e}_{x_j} the orthonormal unit vectors of the coordinate system. $\nabla \times \vec{V} = \text{rot} \vec{V}$ describes the rotation of a vector field; $\nabla \cdot \vec{V} = \text{div} \vec{V}$ its divergence. \vec{B} and \vec{H} , and \vec{D} and \vec{E} , respectively, can be related by two complex constants characterizing the electromagnetic properties of the medium, the complex magnetic permeability μ^* and the complex dielectric constant ε^* :

$$\vec{B} = \mu^* \vec{H}, \quad (2.5)$$

$$\vec{D} = \varepsilon^* \vec{E}. \quad (2.6)$$

The two terms in equation 2.1 represent the displacement and the conduction current, respectively, which both contribute to the total current generating a rotational magnetic field. The displacement current $J_d = \partial \vec{D} / \partial t$ depends on frequency, while the conduction current $J_c = \sigma \vec{E}$ is constant in respect to frequency.

The real part of the dielectric constant, the electrical permittivity ε' contains the permittivity of the vacuum ε_0 and the relative electrical permittivity of the medium ε'_r . The imaginary part ε'' is the dielectric loss factor expressed by the electric conductivity σ of the medium and the circular frequency ω :

$$\varepsilon^* = \varepsilon_0 \varepsilon_r^* = \varepsilon' - i\varepsilon'' = \varepsilon_0 \left(\varepsilon'_r - i \frac{\sigma}{\varepsilon_0 \omega} \right), \quad (2.7)$$

with $i = \sqrt{-1}$. Ice is non-magnetic, hence it follows that its complex magnetic permeability can be taken as real and equal to the one of vacuum,

$$\mu^* = \mu_0 (\mu_r)^* = \mu_0. \quad (2.8)$$

With the assumption of harmonic fields the wave equations derived from the Maxwell equations read

$$\Delta \vec{E} + k^2 \vec{E} = 0, \quad (2.9)$$

$$\Delta \vec{H} + k^2 \vec{H} = 0, \quad (2.10)$$

2.2. The dielectric properties of snow and firn

where $\Delta \equiv \nabla \cdot \nabla = \sum_{j=1}^3 \left(\frac{\delta^2}{\delta x_j^2} \right)$ is the Laplace operator and ik the complex wave number taking into account the electromagnetic properties of the medium:

$$ik = \sqrt{i\mu^*\omega(\sigma + i\varepsilon^*\omega)}. \quad (2.11)$$

At low frequencies the imaginary part of k dominates, at high frequencies the real part, while the imaginary part acts as a damping factor. The transition frequency ω_t , typically in the kHz-range separates the low frequency range characterized by diffusion from a higher frequency range in which wave propagation dominates. The latter one is also referred to as the low-loss regime.

A solution of the above wave equation 2.9 has the form of an harmonic planar wave:

$$\vec{E} = \vec{E}_0 e^{i(\omega t - kz)} \quad (2.12)$$

The attenuation of the wave is generally expressed as the loss-tangent

$$\tan\delta = \frac{\varepsilon''}{\varepsilon'} = \frac{\sigma}{\omega\varepsilon_0\varepsilon'_r}. \quad (2.13)$$

This equation indicates the importance of the conductivity σ in the attenuation of an electromagnetic wave, and the limitation of electromagnetic surveys in well conducting media.

2.2. The dielectric properties of snow and firn

A solid knowledge of the electromagnetic properties of snow, firn and ice is of fundamental importance in the interpretation of radar measurements in Glaciology. Permittivity and conductivity control the velocity of propagation and the attenuation of electromagnetic waves through a medium. Polar snow, firn and ice are generally considered as low-loss regimes ($\sigma O(10^{-5} \text{ S m}^{-1})$), allowing deep penetration of radar waves at frequencies in the MHz to GHz ranging from several meters for the highest frequencies used, up to kilometers of ice for lower frequencies. Reflections from a volume of snow and firn are attributed to variations of the real part of the dielectric constant, the permittivity, and mainly related to changes in density (Wolff, 2000). Variations in the imaginary part, proportional to the conductivity, dominate

2. Theory of Electromagnetic Wave Propagation in Snow and Firn

reflections from pure ice (Glen and Paren, 1975; Richardson-Näslund, 2001; Eisen, 2003). Changes in crystal fabric have also been reported of causing reflections. For the rest of this thesis, the term permittivity will always refer to the real part of the relative dielectric constant (ϵ'_r). For simplicity it will be denoted as ϵ' . Table 2.1 lists permittivity, conductivity and depending parameters of propagation for ice and other common earth surface materials.

Table 2.1.: Typical electrical properties of various common earth surface materials. Modified from Hubbard and Glasser (2005).

Material	Electrical permittivity (ϵ')	Electrical conductivity (σ , mS m ⁻¹)	Velocity (v, m μ s ⁻¹)
Air	1	0	300
Ice	3.14-3.18	0.01	168
Fresh water	80	0.5	33
Salt water	80	3000	10
Dry sand	3-5	0.01	150
Wet sand	20-30	0.1-1.0	60
Silt	5-30	1-100	70
Clay	5-40	2-1000	60
Granite	4-6	0.01-1	130

The dielectric properties of dry snow and firn are derived from those of ice, using mixing formulas, which are discussed first, starting with a brief discussion of the molecular physics of ice. The structure of ice formed under natural conditions ¹ is known as ice 1h, an open hexagonal arrangement following the so-called Bernal-Fowler rules:

1. two hydrogens are connected to every oxygen
2. one, and only one hydrogen is situated between a pair of oxygens, and closer to one than the other

However, natural ice is imperfect and several point defects occur. Positive and negative ionic defects are connected to the violation of the first Bernal-Fowler rule,

¹ Ice which is formed at atmospheric pressure and temperatures of $-100^\circ\text{C} < T < 0^\circ\text{C}$ (Petrunko and Whitworth, 1999).

2.2. The dielectric properties of snow and firn

where one or three hydrogens are connected to an oxygen instead of two, resulting in the formation of H_3O^+ or HO^- ions, respectively. As a violation of the second rule bonds with no or two hydrogens can exist. These are referred to as L or D Bjerrum defects.

The electric permittivity of ice is thought to be connected to the reorientation of water molecules which have a large dipole moment. In absence of an external field the dipoles are randomly orientated, but in the presence of an external field they align in a particular direction. Glen and Paren (1975) pointed out, that it is these infringements of the Bernal-Fowler rules – the occurrence and migration of point defects – which allow the water molecules to turn around and to respond to the presence of an external field. The electric permittivity of pure ice is typically in the range from 3.14 to 3.18 (high frequency limit). The permittivity of pure polycrystalline ice with a density of $\rho_i = 917 \text{ kg m}^{-3}$ at a temperature of around -20°C is well represented by a value of 3.15 (Kovacs *et al.*, 1995).

The conduction of a steady dc-current or very slow alternating current through ice involves the diffusion of charge carriers – ionic or Bjerrum defects – over large distances. According to Ohm’s Law the static conductivity σ_s is given by the ratio of the current density and the strength of the external electric field. The conductivity at high frequencies depends on the imaginary part of the dielectric constant, and is given by $\sigma = \omega\varepsilon_0\varepsilon''$. The conductivity of ice is very sensitive to ionic impurities and generally increases with increasing impurity content. The effect of ionic impurities on the permittivity is, however, small (Dowdeswell and Evans, 2004). As stated above, the dielectric properties of dry snow and firn can be derived from those of ice. Considering simple mixture models like the one from Looyenga (1965), empirical relationships between the permittivity and density of snow and firn have been established. Low-density snow is represented by an inclusion of ice spheres in air, and snow and firn with a higher density by spherical inclusions of air in ice. The classical relationship derived by Looyenga (1965) is used as a standard and reads

$$\varepsilon^{1/3} - \varepsilon_1^{1/3} = \nu(\varepsilon_2^{1/3} - \varepsilon_1^{1/3}), \quad (2.14)$$

where ε'_1 and ε'_2 are the permittivities of the dielectric components one and two, and ν the volume proportion of the second component.

2. Theory of Electromagnetic Wave Propagation in Snow and Firn

In the case of air as the first dielectricum ($\varepsilon'_1 = 1$) and ice as the other ($\varepsilon'_2 = \varepsilon'_i$), equation 2.14 becomes

$$\varepsilon'^{1/3} - 1 = \nu(\varepsilon_i'^{1/3} - 1) \quad (2.15)$$

and ν is now the ratio of the density of snow to that of ice (ρ_s/ρ_i). Experiments verified that the permittivity of snow is almost solely dependent on density (Tiuri *et al.*, 1984). Robin (1975) came up with an empirical equation based on bore-hole interferometric measurements:

$$\varepsilon' = (1 + 0.000851\rho_s)^2, \quad (2.16)$$

with ρ_s in kg m^{-3} . The dimensionless permittivity as predicted by Robin's empirical relation, based on the mixture model from Looyenga (1965), is plotted against density in Figure 2.1. Robin's equation plots as a line from a permittivity of 1, for a density of air ($\rho \approx 0 \text{ kg m}^{-3}$), to a permittivity of 3.15, for a density of 917 kg/m^3 , the value for a permittivity of ice at a temperature of -20°C .

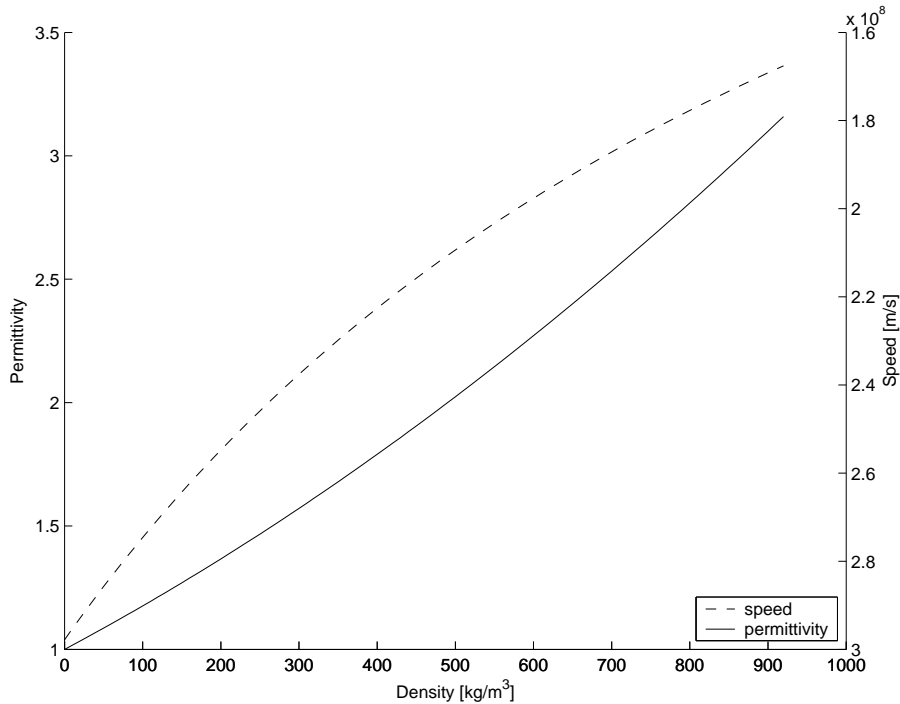


Figure 2.1.: Permittivity of snow, firn, and ice as a function of density according to Kovac's refinement of Robin's equation (2.16) and consequent speed of propagating electromagnetic waves. Note inverse ordinate of wave speed.

2.3. Propagation of electromagnetic waves in snow and firn

Kovacs *et al.* (1995) later confirmed equation 2.16, but suggested a refinement based on a statistical fit to data, and which has become a widely used expression:

$$\varepsilon' = (1 + 0.000845\rho_s)^2. \quad (2.17)$$

2.3. Propagation of electromagnetic waves in snow and firn

The propagation of electromagnetic waves through a medium not solely depends on the dielectric properties. Geometric factors, wavefront spreading, refraction and antenna considerations, as well as reflections and volume scattering from within the medium have to be taken into account (Dowdeswell and Evans, 2004).

In a low-loss regime like dry snow and firn the imaginary part of the dielectric constant is small compared to the real one. Kovacs *et al.* (1995) reported values of the loss tangent $\tan\delta \ll 0.1$ for polar firn. The loss factor is therefor negligible and the velocity of a propagating electromagnetic wave can be expressed by

$$v = \frac{c}{\sqrt{\varepsilon'}}, \quad (2.18)$$

or in terms of the refractive index $n = \sqrt{\varepsilon'}$ as

$$v = \frac{c}{n}, \quad (2.19)$$

where $c = 299.7925 \text{ m } \mu\text{s}^{-1}$ is the velocity of an electromagnetic wave in vacuum.

Table 2.2.: Velocities of electromagnetic waves in ice, after Dowdeswell and Evans (2004). Values are given in $\text{m}/\mu\text{s}$

	1-100 MHz	100 MHz-10 GHz
0°C	167.6 ± 0.6	168.2 ± 0.3
-50°C	168.6 ± 0.6	169.2 ± 0.3

2. Theory of Electromagnetic Wave Propagation in Snow and Firn

With a permittivity of ice ($\epsilon' = 3.15$) the velocity becomes $c = 168.9 \text{ m}/\mu\text{s}$. This value has been confirmed by field measurements, slightly varying with temperature of the ice and the frequency used (see table 2.2).

Direct techniques calculate velocities from permittivity profiles obtained from high-resolution dielectric profiling (DEP) ice core data or by employing permittivity-density relationships from the mixture models. Indirect techniques include bore-hole radar interferometry (Robin, 1975) and common mid-point surveys, a technique commonly used in seismic exploration (Telford *et al.*, 1990). Analyzing data from Dronning Maud Land, Antarctica, Eisen *et al.* (2002) showed that for higher frequencies, density based velocities according to Looyenga's mixture model and Robin's and Kovacs' empirical expressions differ by less than 1% from those derived by DEP.

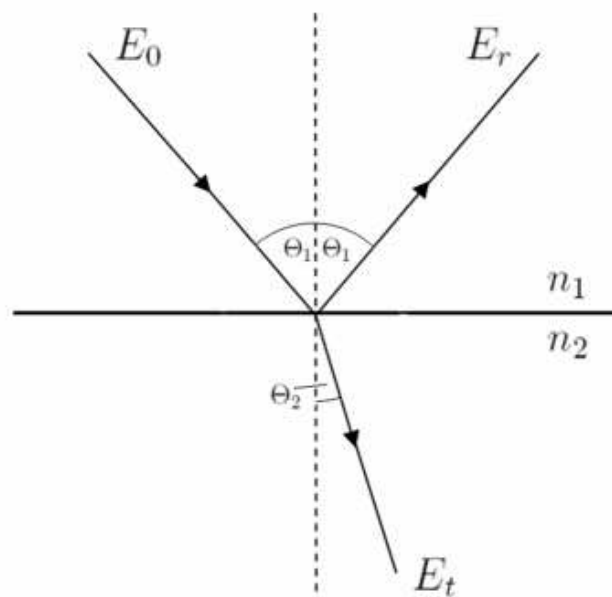


Figure 2.2.: Ray-path geometry for incoming (E_0), reflected (E_r) and transmitted wave (E_t)

Effects at boundaries separating two media (medium 1 and medium 2) with different dielectric properties can be described in analogy to optics. Incoming, reflected and transmitted ray lie in the same plane. The reflection angle is equal to the in-

2.3. Propagation of electromagnetic waves in snow and firn

incidence angle (Figure 2.2). According to Snell's law, reflection and refraction of an electromagnetic wave will occur, in dependence on the incidence angle θ_1 :

$$\frac{\sin\theta_2}{\sin\theta_1} = \frac{n_1}{n_2} = \frac{\sqrt{\varepsilon'_1}}{\sqrt{\varepsilon'_2}} \quad (2.20)$$

The wave is refracted towards the normal, if the permittivity of the second medium is larger than the one of the first. At normal incidence the wave is not refracted. Total reflection occurs at incidence angles greater or equal to the critical angle $\theta_1 = \theta_c$ ($\theta_2 = 90^\circ$) determined by:

$$\sin\theta_c = \frac{n_2}{n_1} = \frac{\sqrt{\varepsilon'_2}}{\sqrt{\varepsilon'_1}} \quad (2.21)$$

No energy is transmitted through the interface. A real solution for θ_c exist only, if $\varepsilon'_2 \leq \varepsilon'_1$. In the case of an air/ice interface it occurs only for waves, reflected at internal horizons and propagating back to the surface. In that case, ε'_2 denotes the permittivity of air, and ε'_1 the permittivity of ice, and the critical angle becomes $\theta_c \approx 34^\circ$.

The amplitude ratio of the incoming and the reflected wave, and the incoming and the transmitted wave, respectively, is generally described in terms of the reflection coefficient R and the Transmission coefficient T :

$$R = \frac{n_1 - n_2}{n_1 + n_2} = \frac{\sqrt{\varepsilon'_1} - \sqrt{\varepsilon'_2}}{\sqrt{\varepsilon'_1} + \sqrt{\varepsilon'_2}} \quad (2.22)$$

and

$$T = 1 + R \quad (2.23)$$

In addition to the dielectric loss discussed above, attenuation of the electromagnetic wave is introduced by spherical divergence, attributed to the distribution of energy over an expanding sphere and proportional to the squared distance from the source; by refraction and volume scattering ('clutter') and by reflection of energy from internal horizons or discontinuous structures of strong dielectric contrast to the volume they are embedded in.

2.4. Ground-penetrating radar (GPR)

2.4.1. Basic principle

A transmitting antenna is excited by a voltage pulse, a sudden application of a short power signal. Voltage and current-waves propagate along the wires and generate an electromagnetic field. An electromagnetic pulse is emitted and penetrates the snow and ice. Part of the signal's energy is reflected at inhomogeneities within the volume or by the bedrock, where the dielectric constant ϵ^* suddenly changes. The reflected signal is detected by a receiving antenna, usually oriented parallel to the transmitting antenna. The signal is recorded as a function of two-way traveltime, the time difference between transmission and reception of the signal. Knowing the velocity of propagation within the medium, it is possible to convert the measured time to depth (Bogorodsky *et al.*, 1985).

The first signal arriving at the receiving antenna is the direct wave, which travels directly above the surface through air. This direct wave signal is strong and leads to interferences between the antennae, obscuring arrivals from the uppermost part of the snowpack. Because of negligible variations of the direct wave along a traverse, it is useful to determine the time of origin by synchronization (Walford *et al.*, 1986).

2.4.2. Accuracy and resolution

Accuracy is the degree to which an absolute quantity, such as traveltime, respectively depth, can be measured. Resolution denotes the minimum spacing of two objects or events, which can still be separated and independently resolved by the measurement system. In the case of radar measurements, these parameters depend on the frequency, shape and length of the radar signal.

In theory, the ideal radar pulse has the form of a single spike, ultimately sharp in the time- and infinitely broad in the frequency-domain. In practise, a spike of this form cannot be produced. The “technical spike” differentiated by the transmitting antenna can be approximated by a so-called Ricker-wavelet. It consists of a major half-wave, comparable to a sinus, but with adjacent half-waves of highly dampened amplitude. The aim is to create a signal of a single half-wave, with zero-slopes besides it's flanks, and thereby facilitating unambiguous detection of the radar-return signal. If the disturbance by noise is low, the vertical resolution of such

2.4. Ground-penetrating radar (GPR)

a wavelet is in the order of $\lambda/4$, with λ being the wavelength in the medium. This distance determines whether reflections from separate interfaces overlies each-other in a constructive or destructive manner. Constructive overlay results in a broader return signal containing both of the returned peaks, which are therefore not separable. The horizontal resolution depends on the footprint of the radar beam, the first Fresnel-zone in particular. This is the area of the footprint, from where constructive interference of reflections occur. The radar footprint, and the radius of the Fresnel-zone increase with increasing depth. As a rule of thumb, the maximum horizontal resolution is, however, often taken as $\lambda/2$. Hence, the resolution in both vertical and horizontal dimensions improves with increasing frequency. Table 2.3 gives an overview of the resolution of commonly used GPR systems in dependence of antenna frequency. Higher frequencies have the disadvantage of stronger attenuation, and hence shallower penetration depth, as well as decreased signal-to-noise power ratios (S/N-ratios). Small S/N-ratios introduce random errors, which can be reduced by summing up x traces at one location. If the noise is randomly distributed in respect to frequency, so-called white noise, the S/N-ratio is thereby enhanced by a factor of \sqrt{x} .

In general, radar wavelets contain 3 to 4 major half-waves, and it is rather the length of the signal, than the wavelength which determines the resolution. Returns from interfaces, spaced in a distance smaller than half of the signal-length in the

Table 2.3.: GPR-system frequencies commonly used in Radioglaciology and corresponding resolution for near-surface surveys

Center frequency (MHz)	Wavelength in snow* (m)	Maximum resolution [‡]	
		Vertical (m)	Horizontal (m)
2000	0.11	0.03	0.05
800	0.26	0.07	0.13
500	0.42	0.11	0.21
100	2.10	0.53	1.05
50	4.20	1.05	2.10

*at a wave speed of $210 \text{ m } \mu\text{s}^{-1}$

‡assuming an ideal signal and little noise

2. Theory of Electromagnetic Wave Propagation in Snow and Firn

medium, overlies each other and are hardly separable. A 500-MHz signal with 2 major periods ($2\lambda \triangleq 4$ half-waves), has a signal length of 4 ns, corresponding to ~ 0.84 m in snow. The vertical resolution of this setup would be around 0.42 m, instead of 0.11 m as listed in table 2.3.

The accuracy in determining the depth of a reflection is limited by the ability to determine the flank of the first major arrival. This in turn depends on the precision of synchronization of first-arrival times and on the sampling interval used to digitize the traces. The sampling interval ultimately limits the accuracy, but synchronization may vary by a few samples. Additional uncertainty is introduced by a simplified ray-path geometry. Since transmitting and receiving antenna are spaced from each other in a certain distance, the ray path is not strictly orthogonal to the surface, nor to horizontally oriented internal reflection horizons. However, this error is only important for very shallow reflections and decreases exponentially with depth. Richardson-Näslund (2001) estimates this error to ~ 4 % within the upper meter of the pack and already smaller than 1 % at a depth of 2 m. Surface roughness (sastrugi field) also introduces changes in the actual ray-path geometry, in dependence of the antennae inclination. If the depth is expressed in meter, errors in the velocity-depth relation have to be taken into account. According to Eisen *et al.* (2002) density based velocities according to Looyenga's mixture model and Robin's and Kovacs' empirical expression differ by less than 1% from those derived by DEP. However, the spatial variability in snow density has to be considered, reported to be in the order of 5 to 10 % (Richardson-Näslund, 2001), as shown later in this thesis. Last but not least, interpretation of radar images is a subjective process and digitization of horizons may introduce errors on the order of 0.1 m.

3. Field Experiment at the EGIG-Line

In spring 2004, CryoSat ground-truthing experiments were performed on the western flank of the Greenland Ice Sheet. Ground-penetrating radar measurements were made along the lines of a detailed 100 by 100-m² grid net with 10 m line spacing (April 29/30, 2004), and along 1-kilometer long sections forming a square (May 01/02, 2004; Figure 3.1). The survey area is located at point T05

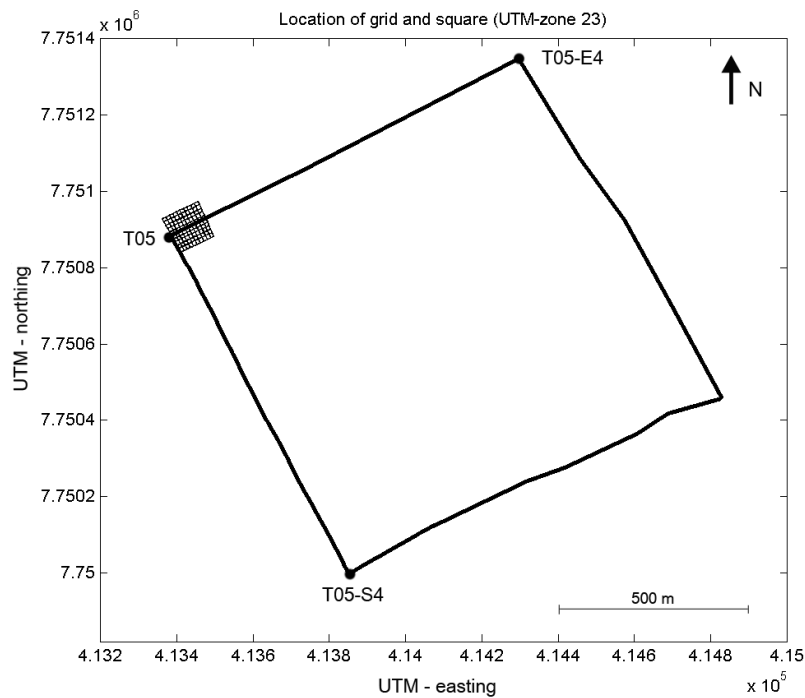


Figure 3.1.: Location of radar profiles forming a 100 x 100-m² grid net and a 1 x 1-km² square (UTM zone 23).

(69° 52' 04.44" N, 47° 19' 59.52" W) of the EGIG-line (see Figure 1.2 in introduction). The altitude of around 1940 m a.s.l. is located within the percolation zone.

3. Field Experiment at the EGIG-Line

In this region surface melting occurs during the summer and melt water percolates into the cold snow pack, where it refreezes to form ice layers, lenses and pipes, causing significant density contrasts in the vertical structure of summer and winter firn (Jezek *et al.*, 1994). Reflections of the radar pulse are attributed to changes in the dielectric constant, which - in dry snow and firn - is controlled by the density contrast (see above section 2.2). Using 500 and 800 MHz antenna frequencies, the aim was to identify and track these near-surface ice layers, affecting the backscatter of CryoSat’s radar altimeter (SIRAL). The GPR-measurements were supplemented by differential GPS and physical snow-properties measurements, derived from snow-pit and firn-core analyses. The ground-based results help to interpret airborne ASIRAS records, sampled along various flight lines across the survey area, and which are directly comparable to CryoSat’s radar altimeter records.

This chapter describes the instruments and the handling of the different data sets. A separate chapter is dedicated to the processing of the GPR data. It represents a fundamental and extensive part of this study. The treatment of GPS, snow-pit and firn-core records is referred to more briefly. These data had been provided by the Institute of Geography at the University of Edinburgh, Scotland. Finally, the data-sets are linked with each-other. GPS measurements allow positioning of GPR profiles in an absolute reference frame.

3.1. Snow pits and firn cores

A stratigraphic record from the survey area was retrieved from nine snow pits and shallow firn cores located in 1, 10, 100 and 1000 m distance east and south from T05—points T05-E1 to E4, and T05-S1 to S4, respectively. At point T05-E3, 100 m east of T05, a longer core (18.9m) was retrieved in addition. The snow pits reached a depth of around 1.45 m. From the bottom of each pit a shallow core with an approximate length of two meters was drilled. The snow-stratigraphic record was made available as (Excel-)tables. Density measurements were performed in steps of visually subdivided stratigraphic units with relative homogeneous properties. Top- and bottom-depth of each unit was noted. The shallow record (~ 3.5 m) also contain a qualitative description of the physical properties—“large crystals, icy firn, snowy firn, etc.”.

3.1. Snow pits and firn cores

To establish a density-depth model, representative for the area of the radar survey, the records of the snow pits and shallow cores falling in the area of the grid were resampled to an equidistant spacing of 5 mm, according to the accuracy of the depth measurement. This method does not alter the original data but allows averaging of the individual density records (see Figure B.1). Below the common depth of the shallow firn cores, the density-depth model is based solely on the record of the long core.

Applying Kovacs' (1995) permittivity-density relation, equation (2.17) and (2.18), the density profile enables the establishment of a velocity-depth model, and consequently a conversion of traveltime to depth. For practical realization, an existing routine, written by Eisen *et al.* (2002) was applied. Density, and wave speed versus depth are displayed in Figure 3.2. In addition, the mean density $\bar{\rho}$ and the mean ve-

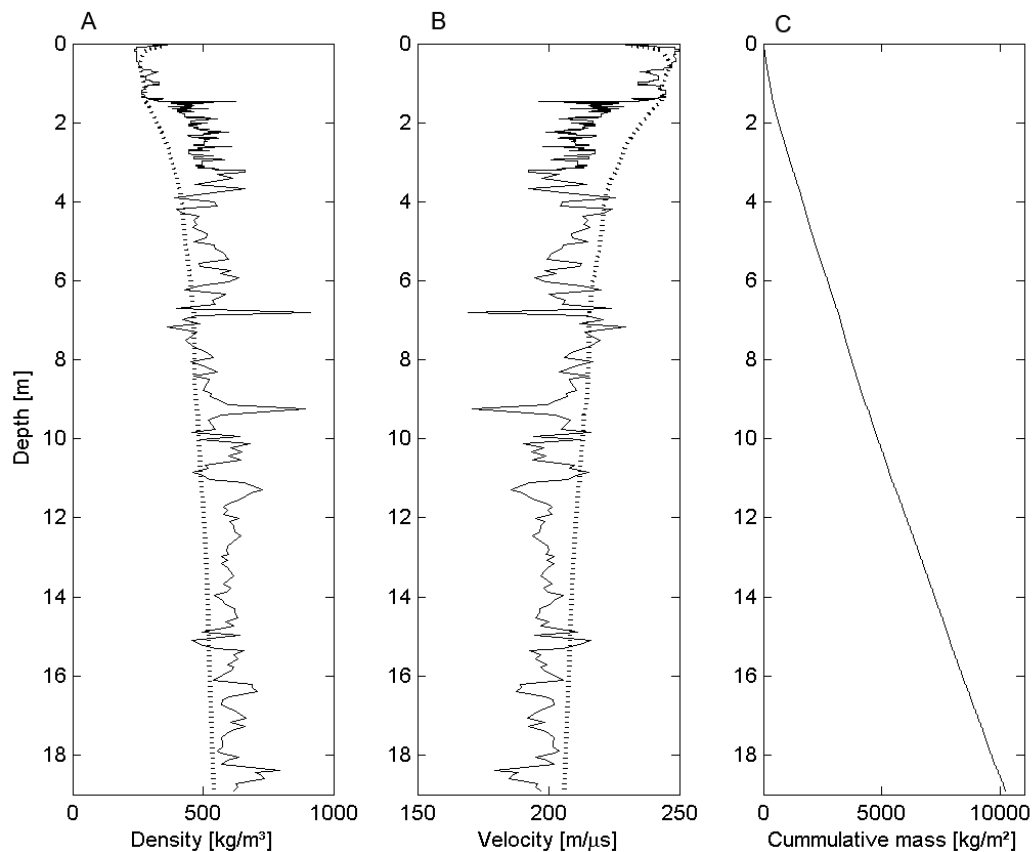


Figure 3.2.: (A) Density-depth relation from in-situ measurements; (B) velocity-depth model, calculated using eq. (2.17) and eq. (2.18). Dotted lines represent corresponding mean values. (C) Cumulative mass as a function of depth.

3. Field Experiment at the EGIG-Line

locity \bar{v} are shown. Both corresponds to the average values for the volume enclosed by the surface and a particular depth. It is the mean velocity, allowing the actual conversion of travelttime to depth ($d = 0.5 \bar{v}t$). Mean values $\bar{\rho}$ and \bar{v} are extremely smoothed versions of ρ and v and therefore insensitive to peaks in the density function. Integration of the density field yields cumulative mass as a function of depth, often expressed in terms of water-equivalent height (m w.e.). However, expression of accumulation in terms of $\text{kg m}^{-2} \text{ a}^{-1}$ is more general and will be used for the rest of the study. These values can be easily translated into m w.e., by simply dividing them by a factor 1000.

3.2. GPR measurements

The GPR data presented here were collected using a commercial RAMAC radar system (Malå GeoScience, Sweden), operating with shielded antennae at center frequencies of 500 and 800 MHz. Altogether 44 profiles are associated with the 100 by 100-m² grid, 22 for each antenna setup; 9 profiles with the 1 x 1-km² square. The odd number results from a gap of around 130 m in one of the long 500-MHz sections, so that this section was treated as two independent profiles. Due to technical problems interrupting the record, long sections are generally a product of several merged profiles of varying length.

The system was mounted on a man-pulled sledge, also hosting a GPS receiver and antenna for simultaneous positing measurements (Figure 3.3). Radar shots were initialized every 10 cm by means of an odometer, a measuring wheel attached to the sledge. To increase the S/N-ratio already during data acquisition, 8 consecutive traces were stacked at each shot-point location. The 8-fold stack was a compromise between measuring velocity and data-quality improvement. At a sampling rate of 0.13 ns, 16 samples cover one wavelength of the 500-MHz signal, and 10 in case of the 800-MHz signal, respectively. A minimum of 8 to 9 samples is required for the proper presentation of one wavelength of a periodic signal. The timewindow, the time the receiver is listening after transmission of a signal, is set to 129 ns corresponding to a depth range in snow of about 13.5 m. Table 3.2 gives an overview of GPR-related survey parameters. The transmitted signal of the RAMAC-GPR consists of about 4 half-waves. According to the general discussion of the accuracy and resolution of

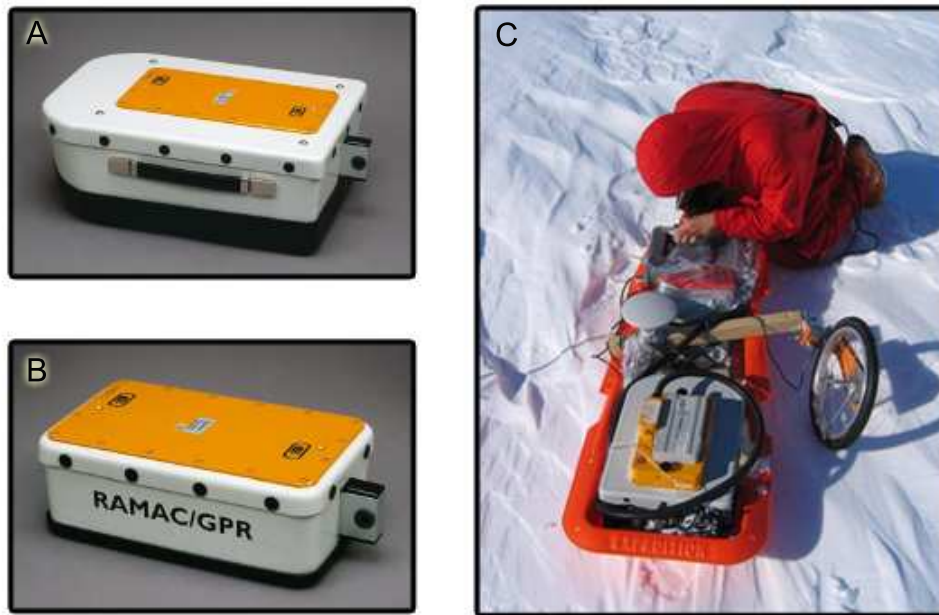


Figure 3.3.: The RAMAC/GPR 500 and 800-MHz shielded antennae (A,B; photos taken from Malå GeoScience’s website (2006)). (C) The radar set in the field. The sledge also hosts a GPS receiver for simultaneous positioning, visible in the center of the sledge.

Table 3.1.: GPR survey-parameters.

Antenna frequency	500 MHz	800 MHz
Antenna spacing	0.18 m	0.14 m
Wavelength in snow*	0.42 m	0.26 m
Signal length	4 ns	2.5 ns
Vertical resolution [#]	0.42 m	0.26 m
Timewindow	129 ns	
No. of samples	1024	
Sampling rate	0.13 ns	
Trace interval	0.11 m	

*at a wavespeed of $210 \text{ m } \mu\text{s}^{-1}$

[#]signal of 4 half-waves

3. Field Experiment at the EGIG-Line

GPR systems in section 2.4.2, the vertical resolution is approximated by half of the signal’s length, which corresponds to one wavelength of the signal in firn—0.42 m in case of the 500-MHz antennae, 0.26 m for the 800-MHz antennae, respectively.

The accuracy in depth measurement is restricted by the ability to determine the arrival of the signal’s first major flank, and by the uncertainty introduced by the conversion of traveltime to depth. The $\lambda/4$ -rule of thumb (0.11 m for the 500-MHz, 0.07 m for the 800-MHz system, respectively) serves as first-order approximation only. The GPR signal experiences modification during propagation throughout the medium. Furthermore the horizons were digitized displaying the envelope, not the original amplitude. As mentioned before, this processing step reduces the frequency content, and hence changes frequency-dependent parameters. In practice, “picking” reflection horizons is a highly subjective process and cannot be exactly quantified. The error at a single point might be as large as the local vertical variation of the reflector. On average, however, we assume that the error does not differ by more than 0.1 m from the depth-location of the real sub-surface feature causing the reflection. This error limit applies for all reflections within the depth range of 13.5 m. Variations in the synchronization of first-arrival times add up to the uncertainty in determining the major return. Variations lie in a range of approximately 3 to 4 samples. On average, the variation is assumed to be in the order of ± 1 sample from the mean, corresponding to about ± 1.5 cm.

The signal is recorded as a function of traveltime. The conversion to depth requires the establishment of a velocity-depth model. In the present study, the model is based on the density measurements from snow pits and firn cores. The density measurement itself can be done with sufficiently high accuracy. The spatial variability in snow density, however, is a source of uncertainty in the velocity-depth model and has to be estimated and taken into account. Here, an analysis of snow pit and firn-core measurements available for the survey area, down to a common depth of 2.5 m was made. The standard deviation of the mean density $\bar{\rho}$ at a certain depth was divided by $\bar{\rho}$, in order to express spatial variability in snow density in percentage from the mean. The variability decreases from about 7 % at 0.5 m depth, to 4 % at a depth of 2.5 m. In the following calculation of error propagation, a constant limit of 5 % was used for the complete near-surface depth range.

The depth d of a reflection horizon is calculated by

$$d = \frac{1}{2}vt = \frac{ct}{2\sqrt{\varepsilon'}}, \quad (3.1)$$

where t denotes two-way-traveltime. The error propagation for the depth computation reads:

$$\sigma_d = \left| \frac{\partial d}{\partial t} \sigma_t \right| + \left| \frac{\partial d}{\partial \varepsilon'} \sigma_{\varepsilon'} \right|, \quad (3.2)$$

with σ denoting the uncertainty. The uncertainty σ_t is negligible, but $\sigma_{\varepsilon'}$ has to be considered. By determining the permittivity ε' using equation 2.17, the error in depth computation can be reduced to the uncertainty σ_ρ in density. Substitution of

$$\frac{\partial d}{\partial \varepsilon'} = -\frac{d}{2\varepsilon'} \quad (3.3)$$

and

$$\sigma_{\varepsilon'} = \left| \frac{\partial \varepsilon'}{\partial \rho} \sigma_\rho \right| \quad (3.4)$$

yields

$$\sigma_d = \left| \frac{ct}{2\sqrt{\varepsilon'}} \frac{\partial \varepsilon'}{\partial \rho} \sigma_\rho \right|, \quad (3.5)$$

which becomes

$$\sigma_d \approx \left| -\frac{d}{2(1 + 0.000845\rho)^2} (1.42805 \cdot 10^{-6} \rho + 0.00169) \sigma_\rho \right|. \quad (3.6)$$

The uncertainty in range computation attributed to the spatial variability of snow density is a function of depth (see Figure 3.4). The error for a reflection depth of 2 m is smaller than 5 cm. For a depth of 5 m it might be as high as 0.1 m, and for a depth of 10 m it may exceed 0.2 m. In relative terms, this translates to an error in depth of 1 to 2 %. If we include the errors, which are approximately constant with depth, the error in depth computation increases from about 0.1 m for reflections within the upper meter, to about 0.3 m for reflections at a depth of 10 m. The order of the maximum error should be kept in mind during discussions of the results. Error values will be, however, not explicitly stated. Table 3.2 lists the maximum errors attributed to the three dominant sources for a set of exemplified IRH-depths. These depth values will be used later on in this thesis (section 6.5).

3. Field Experiment at the EGIG-Line

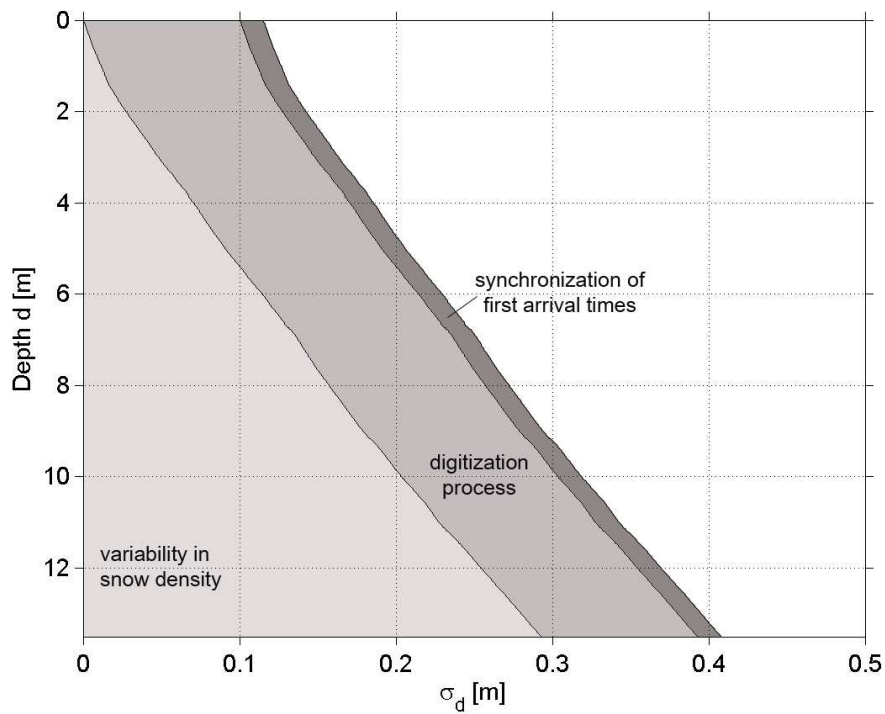


Figure 3.4.: Estimated maximum error in IRH-depth computation for the three dominating contributions.

Table 3.2.: Estimated maximum errors attributed to the three major error sources for a set of exemplified IRH-depths.

Depth (m)	Estimated maximum error attributed to			Sum	
	Vel. model ($\sigma_{\bar{v}}$) [m] [%]	Digitization process [m]	First-arrival Times [m]	$\sigma_{d_{abs}}$ [m]	$\sigma_{d_{rel}}$ [%]
1.61	0.02 1.2	0.10	0.015	0.135	8.4
2.42	0.04 1.5	0.10	0.015	0.151	6.2
3.58	0.06 1.7	0.10	0.015	0.176	4.9
5.34	0.10 1.9	0.10	0.015	0.214	4.0
7.19	0.14 2.0	0.10	0.015	0.256	3.6
10.22	0.21 2.0	0.10	0.015	0.324	3.2

3.3. Differential global-positioning system (DGPS)

The GPS data were supplied in processed form by the Institute of Geography, University of Edinburgh. The data were collected using a Leica instrument. Because the data contained some systematic errors, corrections had to be applied before final processing.

The positioning measurements were performed simultaneously to the radar measurements. Each section was recorded twice; first using the 500-MHz, then the 800-MHz antennae. At the start and end point of each profile a static measurement was made. The sledge was kept in position until variations in GPS coordinates became minimal, thereby achieving higher accuracy compared to the dynamic measurements along track. GPS measurements were triggered every two seconds. So the intervals were equidistant in time, but only equidistant in space (like the radar data), when the velocity during the survey was kept constant. That was not always the case, leading to an inhomogeneity in spatial data density. In order to specify the locations of each single shot, coordinates had been linearly interpolated and resampled in equidistant intervals. The interval length was chosen according to the mean length for the particular profile—profile length divided by number of traces.

Some lines were located on a second surface, with an approximate vertical shift of 2 m above the surface containing the majority of the coordinates. A cross-point analysis of sections representing the same grid-line, recorded on the same day, but lying on both of the surfaces gave a mean vertical displacement of 1.95 m with a standard deviation of 0.17 m. Consequently, profiles lying on the upper surface were shifted downwards by 1.95 m. The residual height differences at the cross-points were in the order of 2-5 cm for profiles recorded on May 29, and up to a few decimeters for profiles collected the following day. The accuracy of the GPS data, especially the vertical coordinate, should therefore be treated with caution.

GPS analysis results that the data set was incomplete. Dynamic measurements were partly missing for four of the grid-profiles. The gap was filled by linear interpolation between the last data point along track and the static start or end-point, respectively. For the long sections, positioning of several profiles was completely missing. Furthermore, along-track data was only available for one line, and just partly for another. However, static measurements existed for the 800-MHz survey, and positions could be interpolated in between. These static measurements had

3. Field Experiment at the EGIG-Line

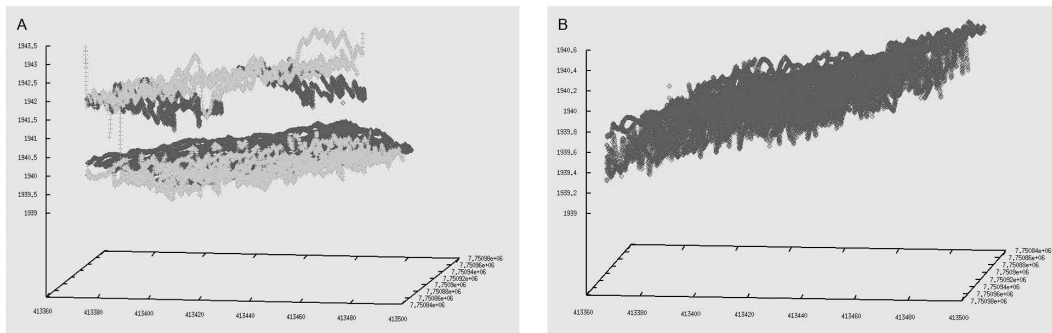


Figure 3.5.: (A) Screen shot of GPS coordinates along grid lines before correction. Light grey markers are associated with 800 MHz, dark grey with the 500 MHz survey.(B) After correction. Note the different vertical scales.

also been used to interpolate shot-point locations for the 500-MHz survey. The gap of around 130 m, existent in one of the long profiles, has been taken into account, too. Interpolation over large distances in the order of several tens to hundreds of meters is assumed to cause negligible variations in the horizontal coordinate, but an unsuitable representation of variations in the vertical coordinate, and hence surface topography. Over the area of the grid, however, the vertical coordinate of the GPS data is assumed to show a realistic trend in surface elevation.

For graphical display of the surface topography, each of altogether 121 cross-points of the grid was given an inverse-distance weighted mean value of the vertical coordinate, including data points within a horizontal range of 3.5 m. The weighting factor linearly decreased from a value of 1 at the exact location of the cross-point to 0 at a range of 3.5 m. Here, the position of “ideal” cross-points were chosen, as marked in Figure 3.6. The actual tracks in the field could deviate up to approximately 1 m from the theoretical grid-points. The four lines, for which shot-point locations had to be interpolated over large distances, are not considered. The same algorithm was applied for the display of internal reflection horizons.

3.3. Differential global-positioning system (DGPS)

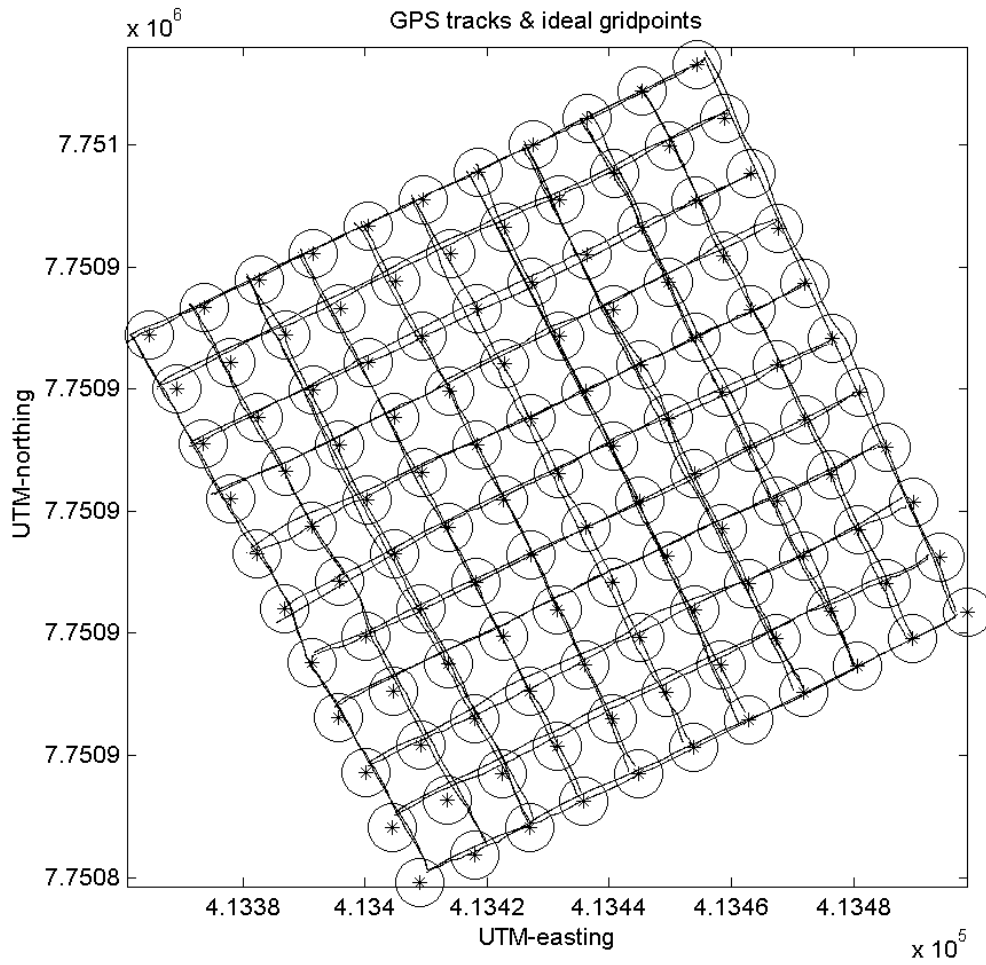


Figure 3.6.: Locations of the grid's ideal cross-points (*) and actual GPS tracks. Circles around the cross-points indicate the area used to determine inverse-distance weighted averages.

4. GPR Processing

The processing of the radar data was performed using Paradigm Geophysics' UNIX-based seismic software packages DISCO and FOCUS (version 5.1). Typical radar velocities, frequencies, and sample intervals differ by a factor of 10^6 from seismic counterparts ($\text{ms}^{-1} \Leftrightarrow \mu\text{s}^{-1}$, $\text{Hz} \Leftrightarrow \text{MHz}$, $\text{ms} \Leftrightarrow \text{ns}$). However, a conversion of RAMAC raw-data into a DISCO-standard format is required. At the AWI, this is done with the RAMACIN module written by Eisen (2003). DISCO is a powerful command line-based program for seismic data processing. FOCUS as add-on supplies the user with a graphical user interface and allows interactive development of the processing flow. Each processing step is realized by either a single or a series of DISCO modules. Once this series of modules is established and the optimal parameters found, it can be saved as a DISCO job. Jobs for different GPR sections have the same structure, but differ in certain parameters, for instance the shot number or the antenna frequency used. Self-developed shell scripts and batch jobs (see Appendix x for `proc.bat` and `dsk2segy.bat`) are practical solutions for automatically creating individual DISCO jobs for all profiles. They extract information from the raw-data file headers by searching for entries which match a certain pattern, and apply them as variables within the source code of a standard job. Figure 4.1 shows the main features of the processing flow. A sample processing job can be found in the Appendix x.

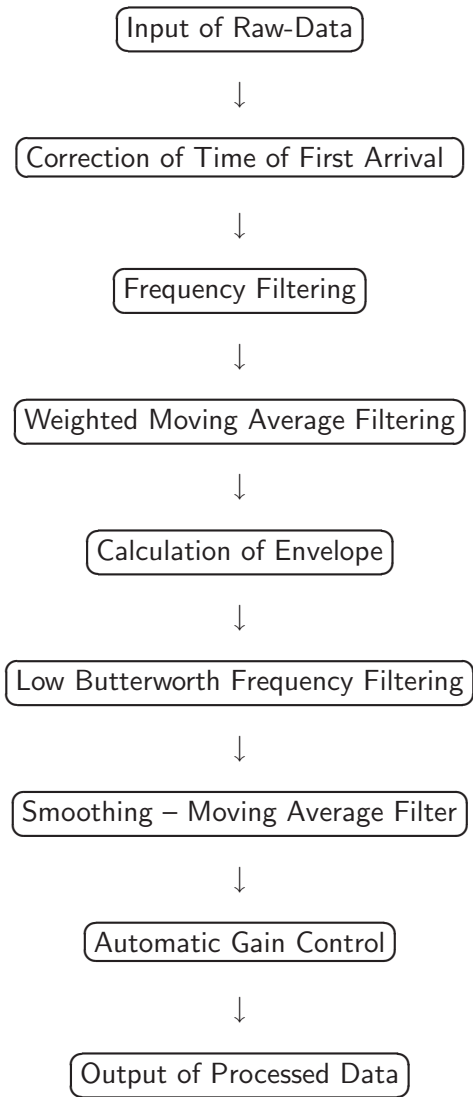


Figure 4.1.: Sketch of DISCO-processing flow for radar data.

4. GPR Processing

4.1. Correction of time of first arrival

This module removes or greatly suppresses continuous drifts and shifts in the first arrival times of individual traces. The range of variation is reduced to about three to four samples. One sample corresponds to 0.13 ns, or ~ 1.5 cm in firn. Continuous drifts can be attributed to variations in battery voltage. Small scale jumps may be introduced by vibrations of the antennae as they are pulled over a rough surface. Large shifts may occur if a number of profiles are merged together into one single profile (Figure 4.2).

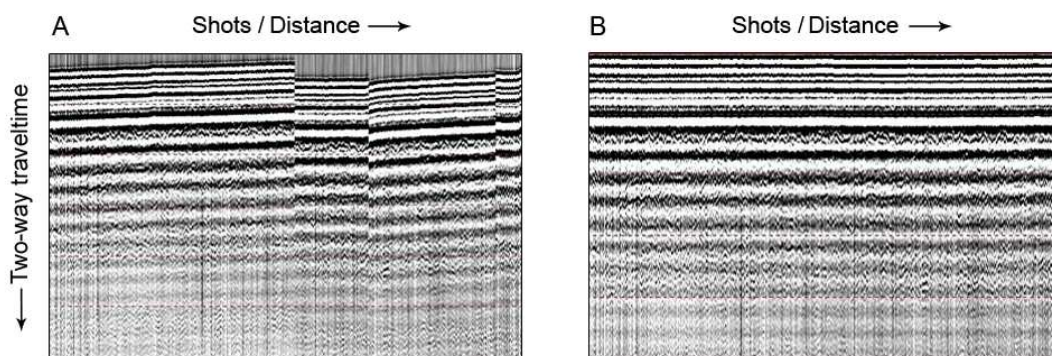


Figure 4.2.: Effect of the correction of first-arrival times displayed for a sample radargram. (A) Before and (B) after shifting of traces.

Shot number and time of first arrival for each single trace were inserted in the header. While the first could be extracted directly from the header of the raw-data, the latter had to be determined with the help of a shell-script routine. Two-way travelttime and amplitude were printed for the first 15 ns of the record, ensuring the signal of the direct wave being enclosed. The time of first arrival was defined as the time at which the actual amplitude exceeds a fixed critical value, suitable for all profiles. This time was set equal to the theoretical time of first arrival; the time needed for the signal to travel directly from the transmitting to the receiving antenna through the air above the surface (0.6 ns for the 500 MHz-system with an antennae-center spacing of 0.18 m, 0.47 ns in case of the 800 MHz-system with an antennae-center spacing of 0.14 m, respectively). The traces were then shifted individually by their corresponding header entry (Figure 4.3).

4.1. Correction of time of first arrival

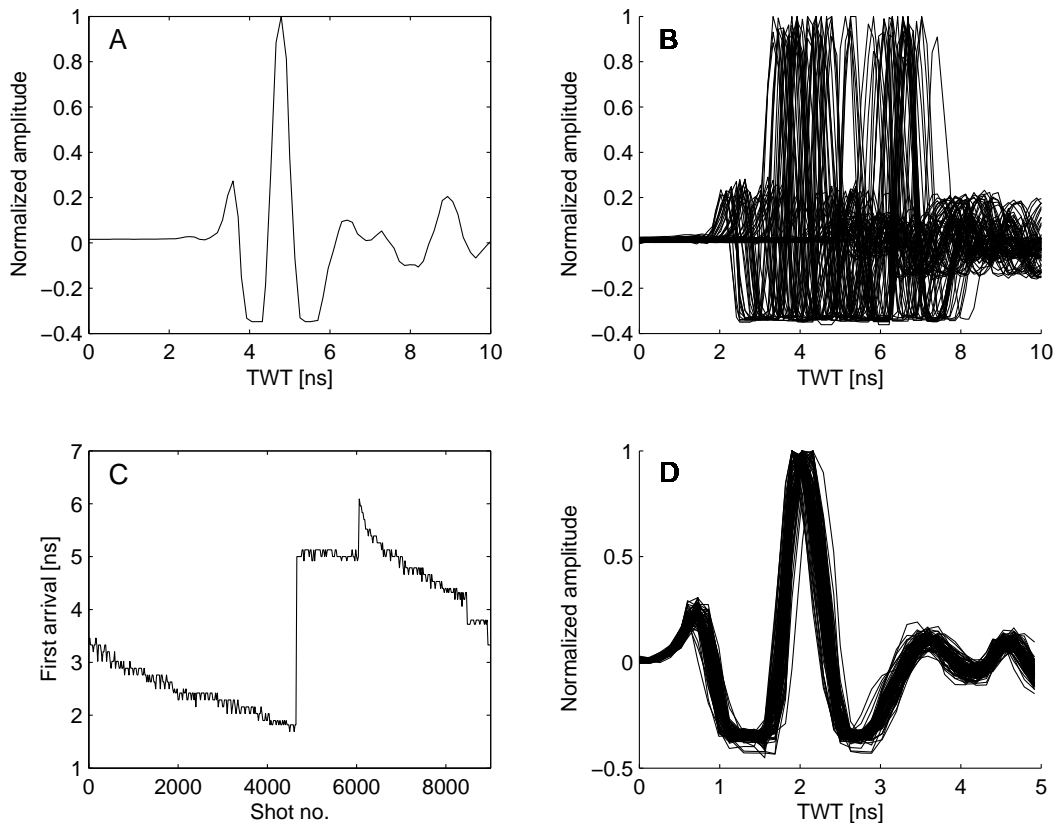


Figure 4.3.: Correction of all shots with respect to their individual first arrival times. (A) Raw signal of a single shot, including the two periods of the direct wave. (B) Every 100th of altogether 9000 uncorrected shots. (C) Times of first arrival, defined by the time at which the amplitude first exceeds a critical value, plotted against shot number; every 20th shot is displayed. (D) Corrected shots. Note different time scale.

4. GPR Processing

4.2. Frequency filtering

Bandpass filtering was performed in the frequency domain with the aim to select a certain range of wanted frequencies and to reject unwanted, in order to suppress noise.

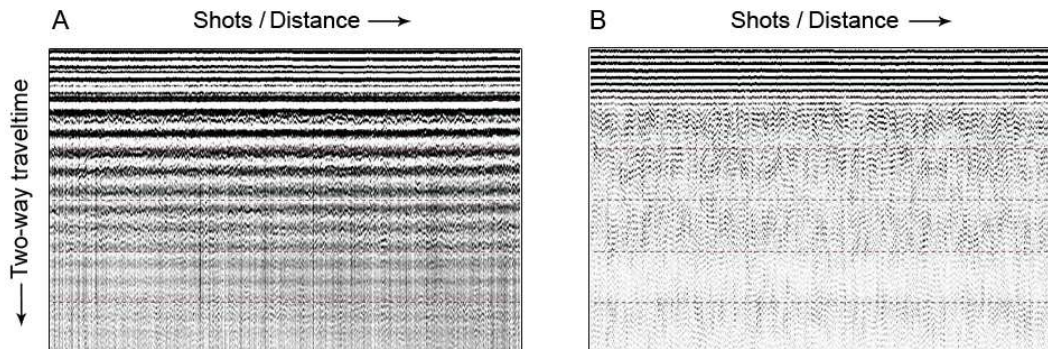


Figure 4.4.: Effect of frequency filtering. (A) Before and (B) after application of the Bandpass filter.

To reduce side lobe effects usually introduced by the sharp cutoff of simple box-car filters, a trapezoidal bandpass filter was applied (Figure 4.4). A trapezoidal bandpass is specified by four frequency values defining the range of frequencies being passed by 100 %, the so-called plateau, and two adjacent tapering windows, throughout which the spectral power is dampened down to zero towards the edges (Mari *et al.*, 1999). Different methods of tapering are available in DISCO. Here, a Hanning-function based on a half-period cosine curve was used. A spectral analysis was performed, using the toolbox implemented in FOCUS. Spectral power was given out in range dB values versus frequency and travel time. Based on the analysis and refined by way of trial and error the frequencies were set to 350/430–680/820 MHz in case of the 500 MHz-antennae, 620/720–950/1100 MHz in case of the 800 MHz-antennae, respectively.

4.3. Moving average filtering

To slightly smooth reflections in the record and to enhance the visibility of possible horizons at an intermediate display a moderate 5-point weighted moving average

filter, with a filter function 0.1, 0.2, 0.4, 0.2, 0.1 was applied in the horizontal direction.

4.4. Complex trace analysis

Complex trace analysis considers the recorded signal as the real part of a complex signal. Applying a non-linear Hilbert transform yields the imaginary part. The envelope corresponds to the magnitude of the complex signal, i.e. its norm. If the envelope is used for processing the information of the polarity and phase is lost. With displaying the envelope reflection bands of the original amplitude record appear more focused and are easier to track (see Figure 4.5). This issue will be discussed in more detail in section 4.7.

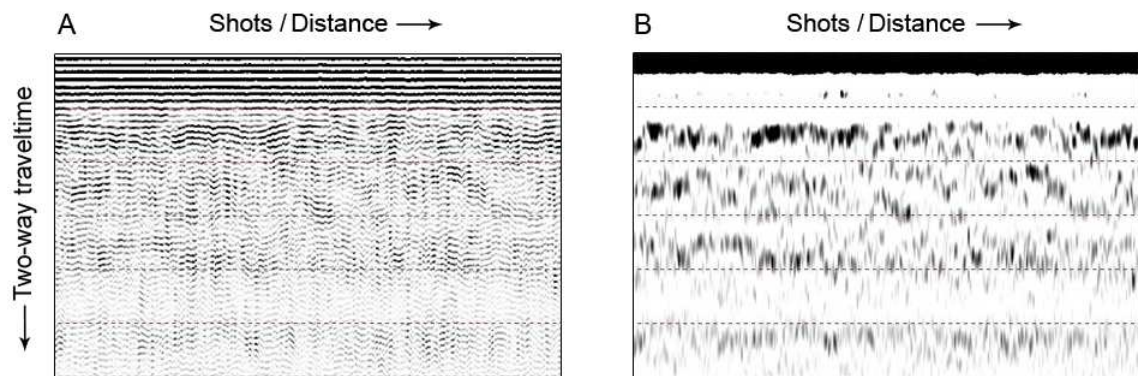


Figure 4.5.: (A) Original amplitude display. (B) After calculation of the envelope and application of a low-frequency bandpass filter.

The envelope is calculated by means of a non-linear Hilbert transformation that significantly reduces the frequency content of the input data and should be followed by the application of a low frequency bandpass filter, especially to remove the DC level and very low frequencies (Paradigm Geophysics, 1995). In this case a Butterworth band pass filter (30-250 MHz) was chosen. Tapering attenuates the signal below and above the plateau by 9dB per octave.

4. GPR Processing

4.5. Final smoothing

To smooth out spikes and to compensate for local weakening of the signal a 5-point moving average filter was applied in the along-track direction. Alternatively, a certain number of traces could have been stacked. Regarding the relatively short profile lengths and the small scale being looked at in this study, stacking would have led to a loss of information, deteriorate resolution, and produced a “blocky” picture.

4.6. Automatic gain

The automatic gain control (AGC) emphasizes low amplitude ranges against ranges with high amplitudes (Figure 4.6). After calculation of the average amplitude of each trace over the whole time window, the amplitudes are scaled such that the mean amplitude within a specified time window equals the average amplitude of the whole trace. The real amplitude information is lost.

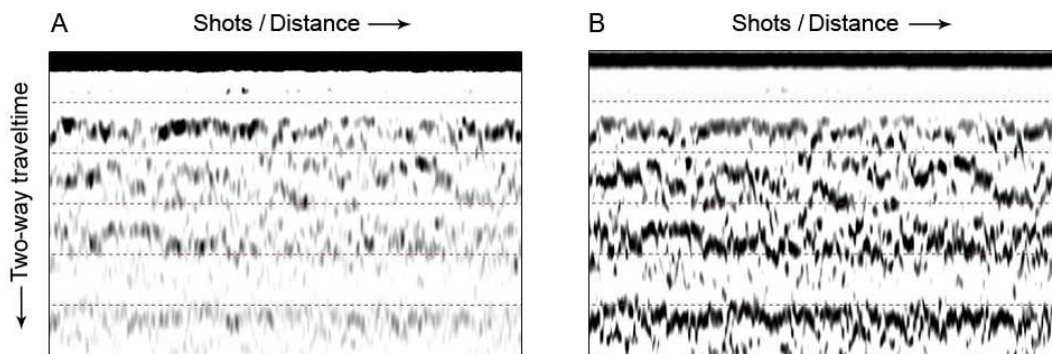


Figure 4.6.: Effect of the automatic gain control, compensating for areas of reduced signal strength

The AGC appeared to be more promising in identifying and tracking single horizons than linear or exponential gain functions compensating for amplitude losses with traveltme, attributed to the distribution of energy over an expanding sphere (Mari *et al.*, 1999).

4.7. Data output

To allow the import of processed data to other software packages the internal DISCO format was converted and output in standard SEG-Y format ¹. Figures 4.7 and 4.8 show the outputs of the original amplitude and envelope for one sample profile. Internal reflection horizons correlate very well with each-other. They appear rather as dark bands of high reflectivity in the amplitude display, but are more pronounced and focussed, hence easier to track in the envelope-display. Therefore, only the envelope was used for following analysis and interpretation.

Previous studies have proven that deterministic deconvolution of radar data may increase the resolution and partly eliminate wavelet interference (Xia *et al.*, 2004). However, own experiments in performing a deconvolution did not improve the quality of the data. One possible explanation is an insufficient model of the source wavelet, as shown in figure 4.3. Xia *et al.* (2004) established a deterministic model of the source wavelet after analyzing the signal traveling through air, assuming a noise-free space. Here, the model of the source wavelet was established from an autocorrelation of the first nanoseconds of the record, containing the direct wave, but also including disturbing effects of the ground coupling and hence convolutional effects with the medium being imaged.

4.8. Interpretation

Enhanced visualization and interpretation was performed using Landmark's seismic-interpretation software package OpenWorks, its application SeisWorks2D, in particular. Semi-automatic picking routines facilitates digitization of internal reflection horizons. Several sections can be displayed simultaneously. Horizons digitized in intersecting profiles are applied and drawn as markers into the current displays, thereby ensuring that the same horizons are tracked in all sections. Visualization of a closed polygon from sections of different profiles provides an additional means of control. The geographical location of the profiles, as well as the corresponding location of the cursor's position within a profile can be controlled in a separate project

¹ standard format of the Society of Exploration Geophysicists

4. GPR Processing

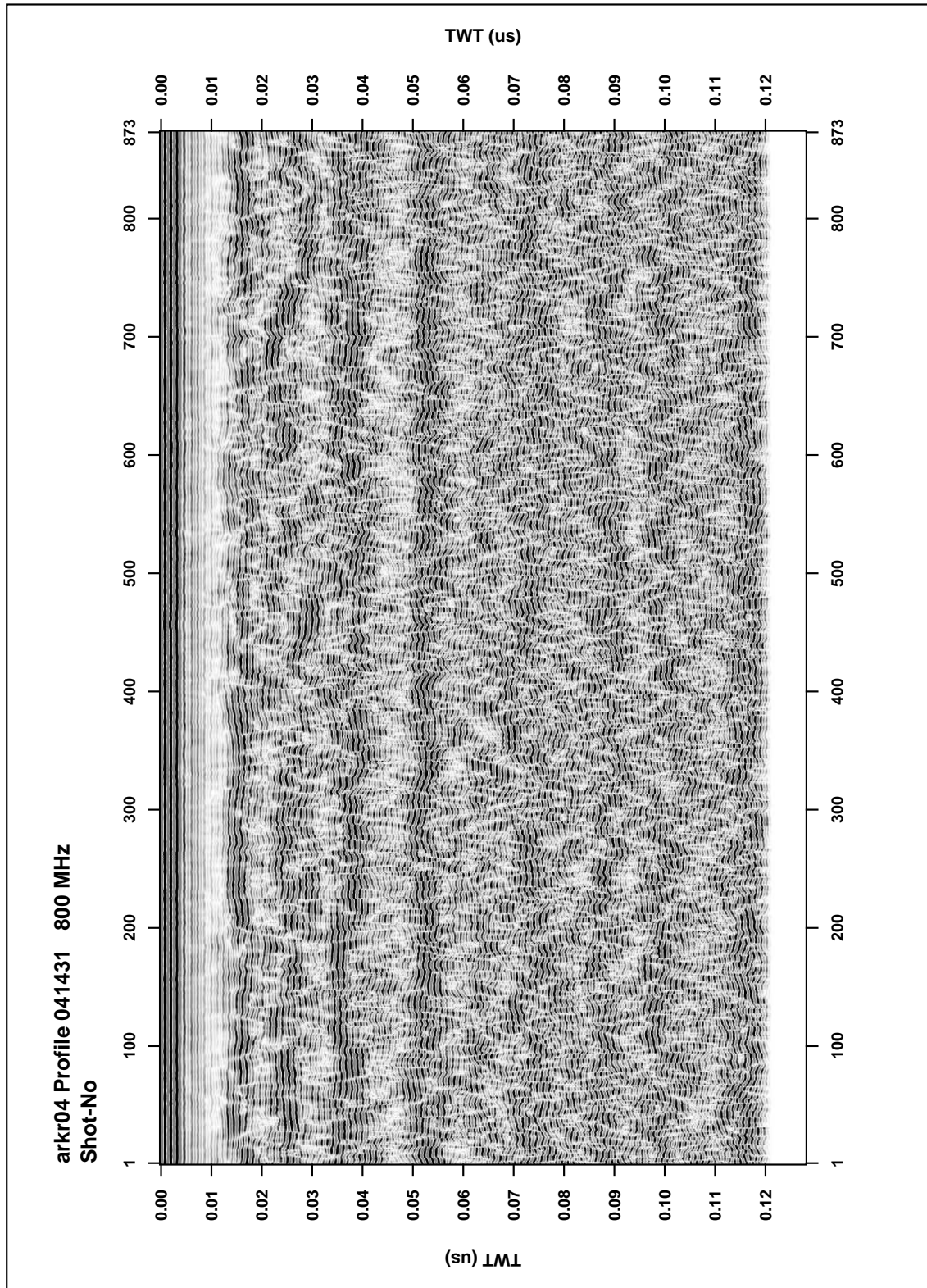


Figure 4.7.: 800-MHz radar section after static correction, filtering and automatic gain control.

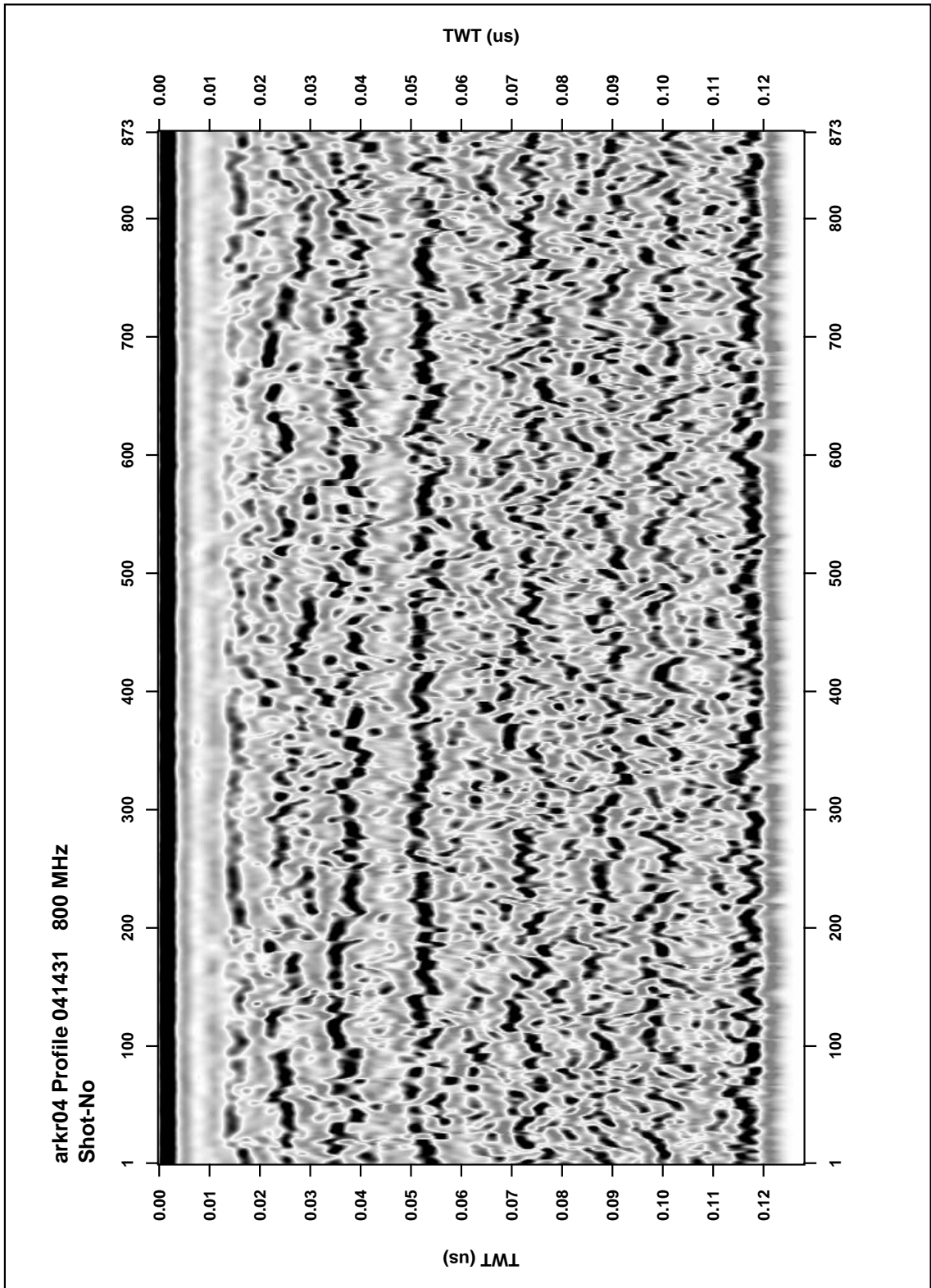


Figure 4.8.: Same 800-MHz radar section as in figure 4.7 after static correction, filtering, calculation of the envelope and automatic gain control.

4. GPR Processing

map. Digitized horizons may be displayed in the map, giving an overview of the interpretation's progress.

To allow loading of the seismic data into Landmark, it had been converted into SEG-Y format. In order to display the data, navigation files are required for all sections. These files consist of a header, containing line-ID, number of shots and the related survey name, a file defining the shot-to-trace relation (important in case of stacking) and a table, specifying the geographical position of each shot in UTM-coordinates. The navigation files were created, utilizing existing routines written by Eisen (2003).

SeisWorks provides the user with numerous predefined colorbars for imaging of seismic data. Colorbars can be manually adjusted, or new ones can be created, alternatively. Color does not change the data itself, but a suitable color range may enhance the visibility of subsurface features significantly. Here, a colorbar ranging from blue over white to red was found to be most convenient. Small values of the envelope are shown in blueish colors, large values in reddish. The colorbar was rescaled for picking the most shallow horizon (the last summer surface). In this case, the signal strength was reduced by the influence of the dominant direct wave in the same AGC-window, and has to be compensated.

An ideal internal reflection horizon appears as a continuous interface on which a seismic attribute is subject to small variations only. The horizon can then be defined as a single line, connecting for example maximum, minimum, or zero amplitude, or the same phase of consecutive traces. With the amplitude being displayed, a well defined reflector appears as a pronounced phase polarity sequence of the three major half-cycles of the signal (+ - + or - + -), depending on whether the reflection coefficient is positive or negative. Reflection horizons in the present radar-data set appear as bands of high reflectivity, rather than as clear interfaces, with numerous, discontinues changes in polarity. The structure of refrozen melt layers within the percolation zone is very complex. The return signal is an integral of the backscatter from a cluster of ice structures, unlikely to be resolved individually. Defining horizons by a single line is therefore a highly subjective and ambiguous process. In an attempt to minimize subjectivity, bands of high reflectivity, thought of as an envelope of the reflection horizon, were digitized by tracking the upper and lower edges of each band, followed by a computation of the centreline. This method provides additional information for interpretation. The band's width, for example, is

a measure of how well a reflector is defined. Horizons within the 100 x 100-m² grid were digitized, using both methods, later referred to as single-line method and band method. Reflection horizons in the 1-km sections were only defined by applying the band method. The horizons were exported from Landmark separately for the 500 and 800-MHz survey. The ASCII-tables containing information of line-ID, shot no., UTM-Easting, -Northing, and traveltimes were later analysed on the basis of Matlab.

5. Results

The objective of this study is to identify internal reflection horizons and to investigate their spatial variability. Internal reflection horizons partly represent features once exposed to the surface, and their detailed description will therefore be preceded by a presentation of the surface topography. After an introduction in the general GPR-data properties, I will discuss the results of the 100 x 100-m² grid. A combination of all 2D profiles allows extrapolation of internal reflection horizons into a 3D space. Results from the 1-km sections follow later. An important aspect is to compare variations on a scale of 1 km with those of a scale one order of magnitude smaller, and to analyze whether there is a trend along the 1-km profiles not observable (or existent) over the area of the grid.

If not explicitly stated, values are an average of both 500 and 800-MHz measurements. A comparison of results, obtained at different antenna frequencies, will be discussed in section 6.1. Mean values of a parameter p are denoted as \bar{p} .

5.1. GPR-data properties

Figure 5.1 shows an arbitrarily chosen 100 m long 500-MHz section, oriented parallel to the slope. The profile represents the same grid-line presented as 800-MHz version in Figures 4.7 and 4.8. The amplitude, and the envelope of the static-corrected, filtered and gain-corrected radargram are shown, as well as upper and lower edges of bands of high reflectivity, digitized utilizing the envelope-display, and their computed centerlines. The timewindow of 129 ns corresponds to a depth range of about 13.5 m. As mentioned before, internal reflection horizons in amplitude- and envelope-display correlate very well with each other, but are more pronounced and focussed in the latter. Spacing between digitized horizons increases with depth, but further horizons can be identified, probably one each between the horizons around 4, 6, and 8 m,

5.1. GPR-data properties

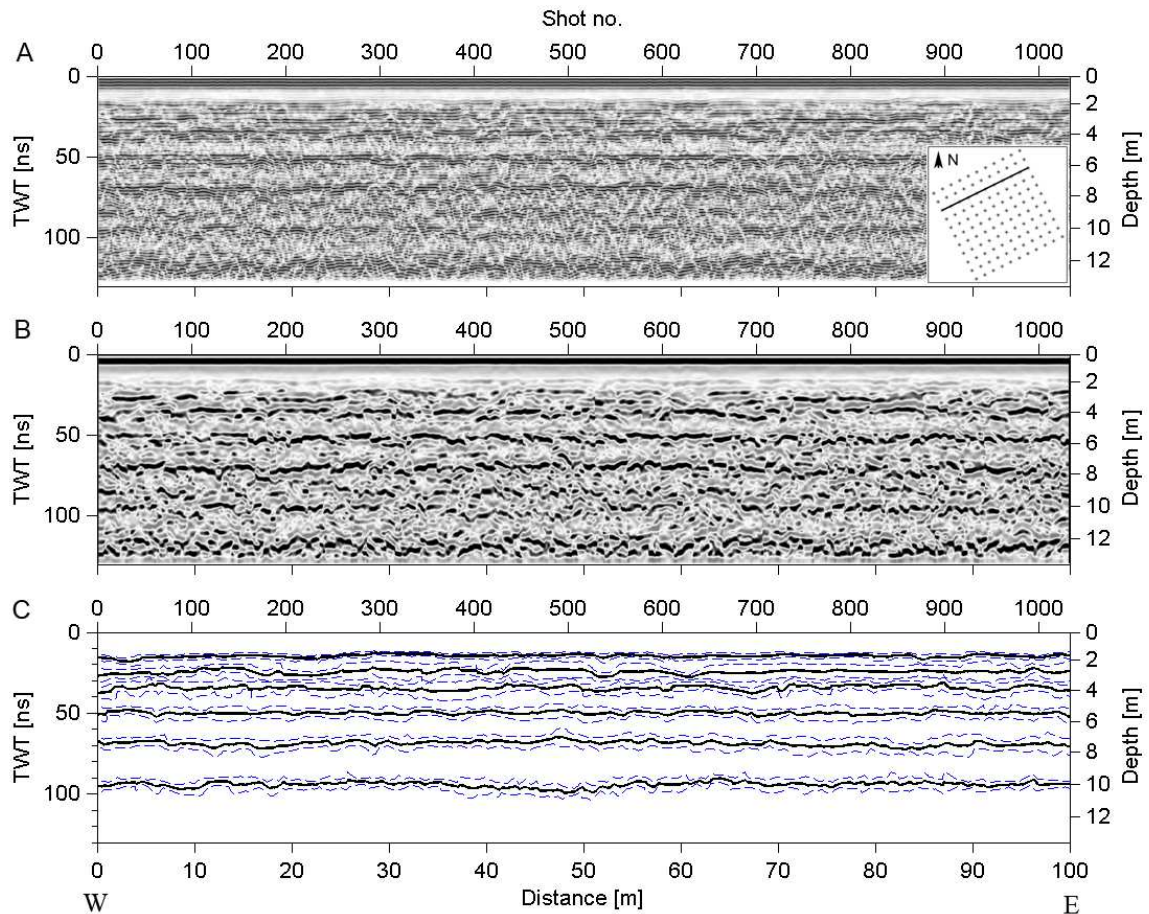


Figure 5.1.: Arbitrarily chosen 500-MHz profile stretching roughly west-eastwards, as indicated in the inlet of (A). Static corrected, filtered and gain corrected radar-gram, displaying the amplitude (A) and the additional calculated attribute of the envelope (B). (C) Digitized bands of high reflectivity (upper and lower edge as dashed lines, computed centerline as solid line). Left-hand vertical scale is two-way traveltime (TWT) in ns, right-hand, converted depth below surface (nonlinear scale).

5. Results

and two between 8 and 10 m. However, these reflection horizons are not clear and strong enough, to be unambiguously and continuously tracked.

Characteristic for all radargrams is a wasted zone, obscuring more than the upper meter of the record. It arises from interference between the strong initial signal of the direct wave, traveling through the air above the ground, the ground wave, which penetrates the snow surface and propagates just below the surface, and a third signal which is reflected at very shallow depths. No information about the subsurface can be obtained within this region. Another effect obscuring shallow features is an artefact caused by the automatic gain, visible as a blanking zone. The AGC scales the amplitudes, such that the mean amplitude within a certain time (depth) window equals the mean amplitude of the full window. Since the direct wave is very strong, the region immediately below is blanked. This effect could partly be compensated during the digitization process by adjusting the colorscale. In addition, a linear gain function was applied tentatively, to ensure that no information was completely lost due to the artefact. The same effect occurs at the very bottom of each radargram. Applying static correction to the traces leaves an area with no data (zero-amplitude) at the end of the timewindow, causing over-representation of the amplitudes at the bottom. The AGC-effect at the bottom probably overlies another true reflection horizon, but is hardly separable from it. This is especially true for the 800-MHz record, which tend to yield significantly larger depth for reflection horizons within the lower parts of the timewindow, as will be discussed in section 6.1.

5.2. Surface topography

The study area is located on the western slope of the Greenland Ice Sheet. Hence the surface elevation at the grid moderately increases east–north–eastward, towards the summit and ranges from 1939.2 to 1940.6 m with a mean of 1940.0 m (Figure 5.2). On top of the general trend, the spline-interpolated surface topography shows small-scale undulations, emphasized by a 20-fold vertical exaggeration.

The predominant wind direction is from east–north–east, controlled by catabatic flow down the ice sheet, parallel to the surface gradient, and driven by gravity. Relatively warm air masses cool in the atmosphere-surface layer and hence densify. Since the terrain is rather flat, it is not expected that this wind field leads to significant

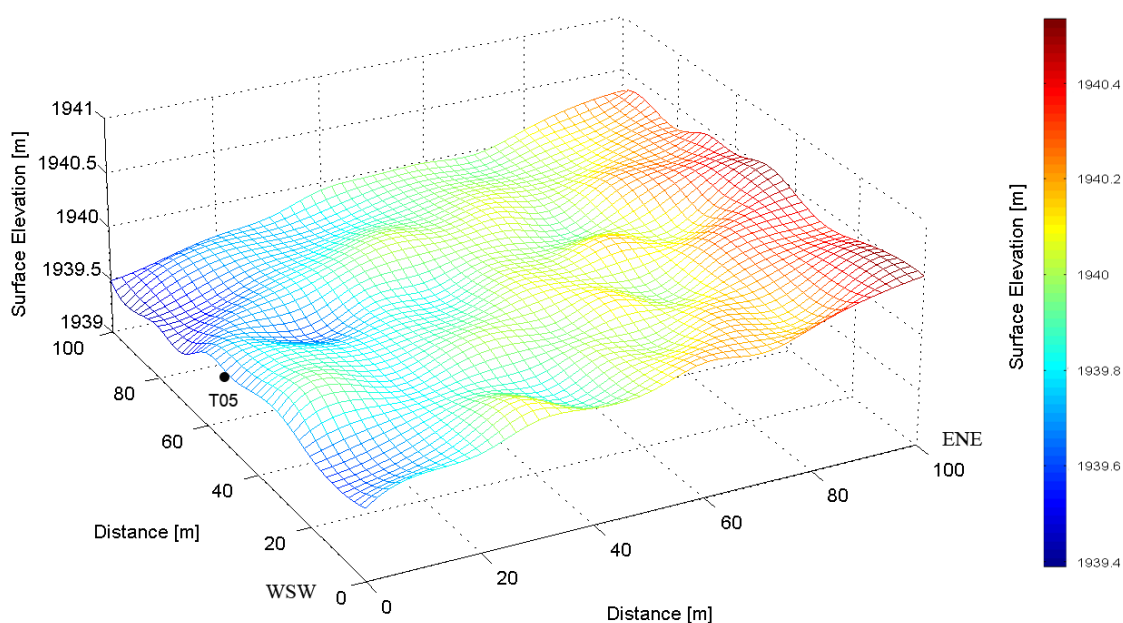


Figure 5.2.: Surface-elevation model for the grid-area viewing from south to north. Vertical exaggeration is 20-fold.

variations in snow accumulation on the local scale of 100 x 100 m. Small-scale drift patterns, called sastrugi, with typical dimensions in the order of decimeters to meters are though present. Sastrugi align in wind direction and indicate recent wind erosion caused by small-scale turbulence in the surface-boundary layer. These features are, however, too small to be resolved (3D) by the surface elevation-model, which is based on inverse-distance weighted means at the grid's crosspoints, as discussed in section 3.3. The undulations rather represent a smoothed pattern superposing the sastrugi field, with characteristic dimensions probably one order of magnitude larger ($O(10\text{ m})$).

5.3. Internal reflection horizons

Altogether six internal reflection horizons down to a depth of about 10 m could be identified and tracked, both within the area of the grid and along the 1 km-radar sections. They will be referred to as IRH-15 to IRH-95, with numbers indicating their approximate depth position in nanoseconds of traveltime.

5. Results

The horizons are relatively flat, almost parallel to each-other and to the gently sloping surface topography, taken as reference level (depth = 0). Over the scale of the grid, there appears no indication of a spatial trend in snow accumulation (Figure 5.3). As for the surface topography, the display of the horizons is based on

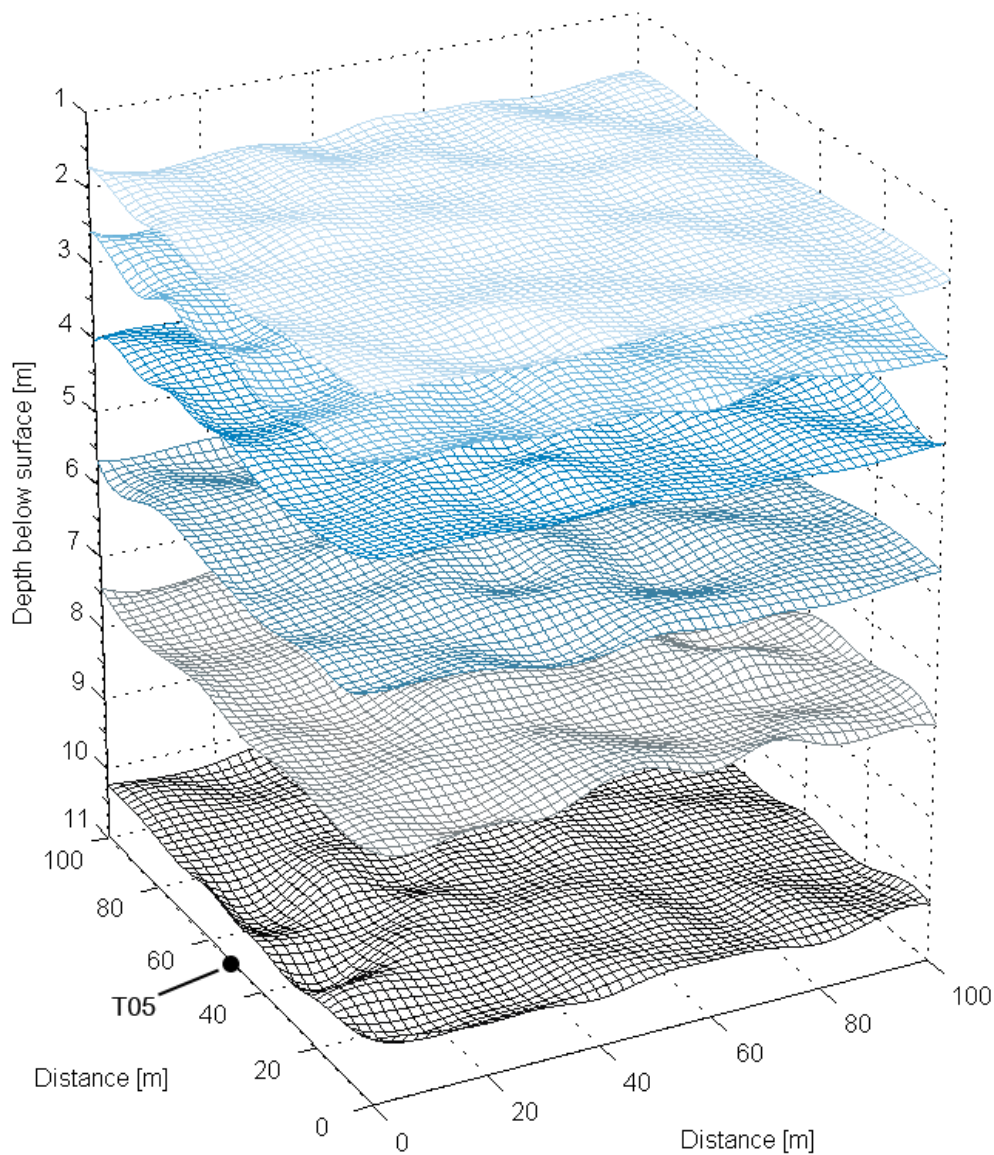


Figure 5.3.: Internal reflection horizons in respect to the surface topography (zero-level), viewing from south to north. Vertical exaggeration is 20-fold.

5.3. Internal reflection horizons

veals signs of a wave-like pattern, best identifiable for the most shallow reflector. About seven crests are stretching roughly from west to east, yielding an average wavelength of about 24 meters (length of the grid-diagonal divided by six wavelengths).

For a more detailed view of selected internal reflection horizons, contour plots of the computed centerline and corresponding bandwidth are plotted for the two most pronounced horizons, IRH-15 and IRH-50 (Figure 5.4). As for the 3D-display, a

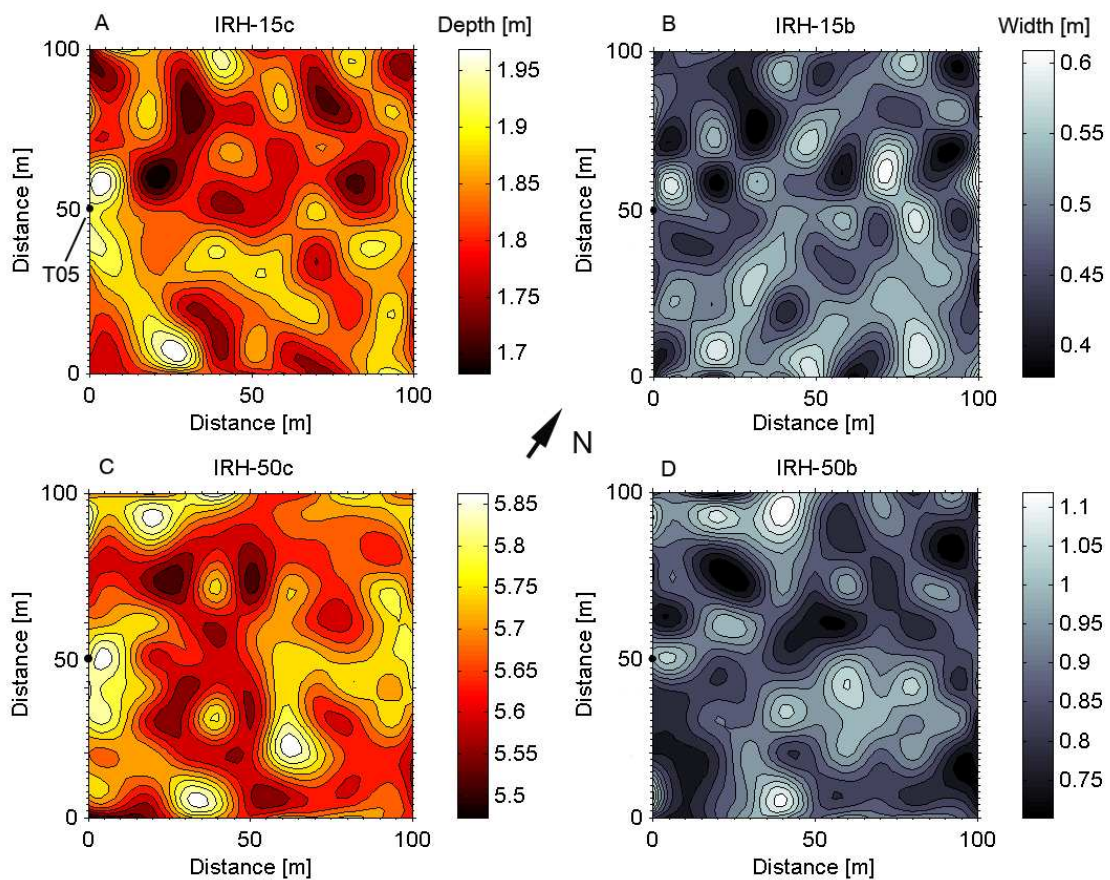


Figure 5.4.: Contour plots of selected internal reflection horizons' depths (centerline) and associated bandwidths, respectively. Last summer's percolation layer (A and B); and horizon around 50 ns traveltime (C and D). Note the direction of North. Contour unit is meter.

spline method was applied to interpolate the surface between the 121 grid-points. The additional plot of the bandwidth on the right-hand side helps to validate and interpret features in the topography of the horizon, plotted on the left-hand side. Undulations in (centerline) topography are often associated with local extremes in

5. Results

bandwidth, since widening of the digitized band arises from encompassing reflection amplitudes, either by extending the upper or the lower limit of the band, and hence shifting the centerline up- or downwards. The wave-like pattern mentioned above can be recognized in the plot of IRH-15, although not as identifiable as in the 3D- display. Amplitudes of these wave structures are in the order of 20 cm. For IRH-50 the wave pattern is hardly apparent. The depth values seem to be more randomly distributed around a mean value. On this scale, for none of the horizons a systematic gradient be made out. The histograms plotted in Figure 5.5 reveal gaussian distributions of depth values around a mean of 1.84 m and a standard variation of 0.11 m for IRH-15; and $5.69 \text{ m} \pm 0.17 \text{ m}$ for IRH-50, respectively. For the bandwidth, there might be a bias towards smaller values. The mean bandwidth for the most shallow and focussed horizon is 0.49 m, and in case of IRH-50, 0.75 m, respectively. The average bandwidth of all horizons is $0.65 \pm 0.22 \text{ m}$, which is in the order of about more than half of the expected thickness of an annual accumulation layer. Histograms of other IRHs can be found in the appendix (Figure C.1).

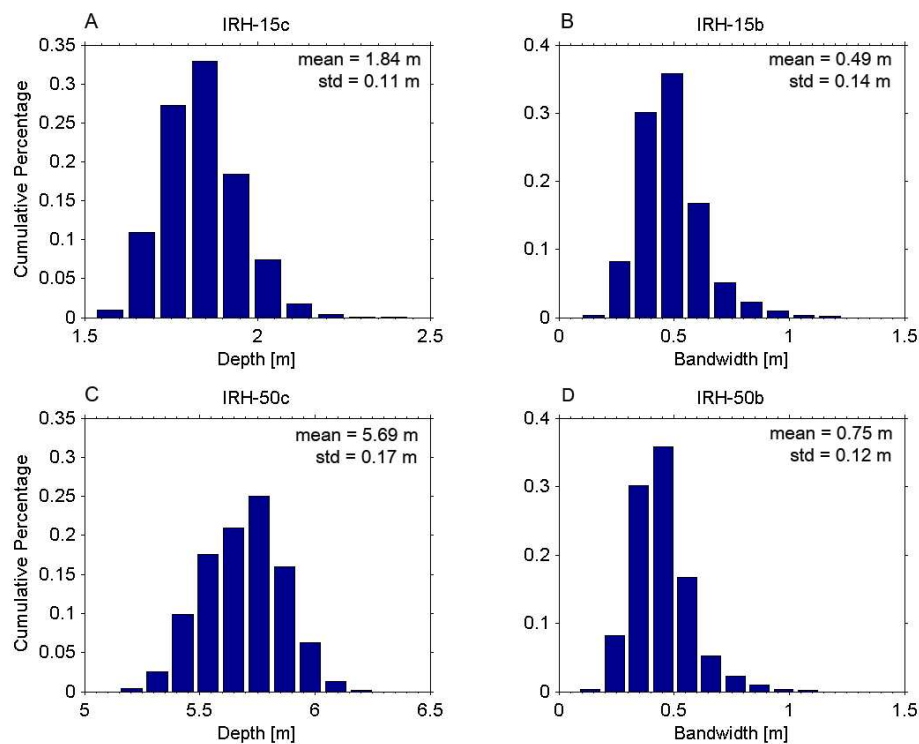


Figure 5.5.: Histograms of IRH-depths and bandwidths for last summer's percolation layer (IRH-15; A and B) and IRH-50 (C and D). Analyses are based on 39715 samples. Values refer to computed centerlines.

5.3. Internal reflection horizons

To identify a possible spatial trend over the area enclosed by the 1 x 1-km² square, inverse-distance weighted mean values had been computed for IRH-depths at mid- and end-points of 1-km sections. The search-radius was set to 100 m. Bars drawn with their base-lines placed at the corresponding point express average layer-depths at the particular point relative to the mean along all 1-km sections (Figure 5.6). They give a first indication of a trend which has yet not been recognized over the area of the grid. Internal reflection horizons seem to dip towards the south-west, implicating a thinning of layers in the down-slope direction. Values range from – 5.2 % at the mid-point of the line connecting point T05 and point T05-S4 to +5.3 % at point T05-E4. The mean layer-depths along the 1 km sections differ, however, by less than 1 % of those derived for the grid (Table C.6).

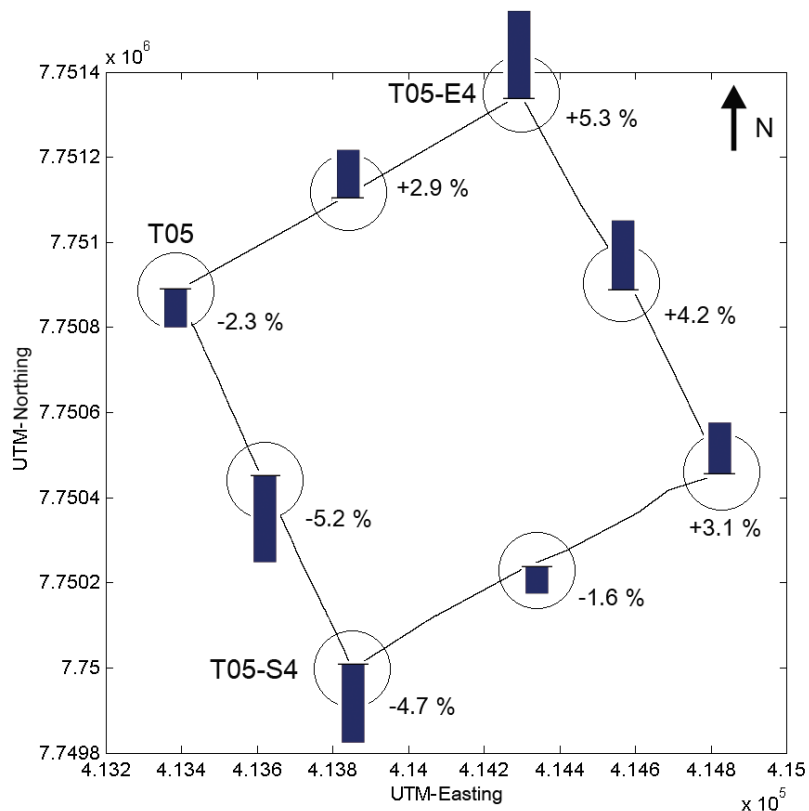


Figure 5.6.: Indication of systematic inclination of internal reflection horizons over area of 1 by 1-km² square. Bars visualize inverse-distance weighted layer depths from points within a search radius of 100 m, relative to the overall mean.

6. Discussion & Conclusions

The spacing between consecutive horizons is a measure of temporal variability in snow accumulation, if their age, and hence the associated time period of accumulation is known. Buried layers are subject to compaction and densification, and spacing between consecutive summer surfaces becomes progressively smaller with depth, if negligible inter-annual variability in snow accumulation can be assumed. For this study, spacing between digitized horizons increases with increasing depth. I attribute this to the fact, that no attempt was made to track events, very poorly constrained, so that periods enclosed by adjacent horizons do not represent the same time span of accumulation. Later in this chapter (section 6.5), I will approximate the age of horizons by considering the mean accumulation rate previously derived from snow-pit and firn-core analyses. Starting with a comparison of the results derived with the two different antenna frequencies, important conclusions can be drawn concerning the evaluation and interpretation of the GPR measurements.

6.1. Frequency dependency of results

Reflection horizons obtained at different antenna frequencies are not a priori attributed to the same real sub-surface feature. The GPR resolution is strongly related to frequency and return echoes are generally an integral of multiple backscatter. However, both records reveal a number of 6 clearly identifiable horizons, located at approximately the same depth (Table C.4 in appendix). It is therefore assumed that they represent the same year's summer-melt layer.

To investigate systematic differences, the distribution of depth ratios of 800 and 500-MHz measurement was computed. Thereby, the 800-MHz results are expressed relative to the 500-MHz results, and differences can be read in percentage. Reflection horizons appear slightly deeper in the 800-MHz survey than in the 500-MHz survey, with an average of 4.8 % (Figure 6.1). The mean position of the most shallow

6.1. Frequency dependency of results

horizons are almost identical. Both surveys yield a depth of 1.84 m for IRH-15 and differ by 0.1 % only. At increasing depth, the 800-MHz measurements yield progressively larger layer-depths with a difference of 6 % (0.52 m) for IRH-95, the deepest horizon at 10.36 m depth. However, maximum relative deviation of 6.9 % occurs for IRH-35 at a depth of 3.99 m, but only translates to about 0.16 m in absolute terms. No trend in respect to depth appears for the ratios of the depth-

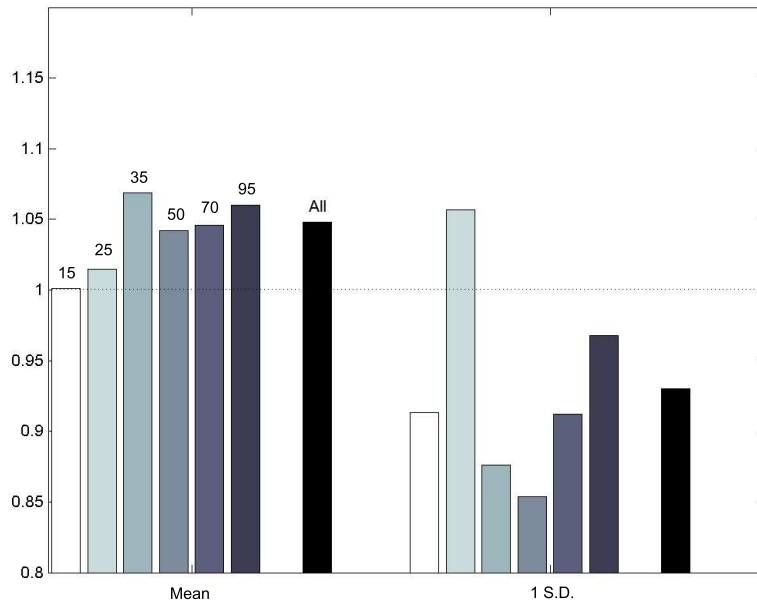


Figure 6.1.: Comparison of antenna frequencies. Plotted are 800-MHz/500-MHz ratios of IRH-depths and corresponding standard deviations. Each horizon is represented by an individual bar. An additional bar gives a mean ratio for all horizons.

standard deviations. Standard deviations are on average 7.0 % smaller for the 800-MHz than for the 500-MHz measurements, and only larger for IRH-25 (+ 5.7 %).

Regarding differences in the width of digitized bands, the 800-MHz survey generally yields larger or similar values, +6.0 % on average. The bandwidth associated with IRH-50 is an exception. It appears 7.9 % smaller than for the 500-MHz system (Figure 6.2). The relative bandwidth's standard deviations seem to be randomly distributed around a value of one. Standard deviations associated with the 800-MHz survey are with +0.9 % very close to the one associated with the 500-MHz survey.

The differences in the bandwidths and corresponding standard deviations are sufficiently small to consider them as independent from the antennae used. The

6. Discussion & Conclusions

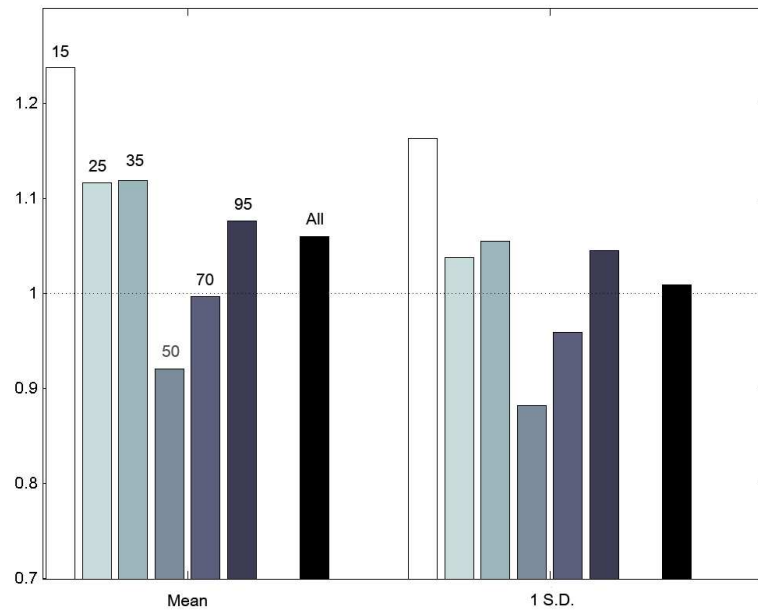


Figure 6.2.: Comparison of antenna frequencies. As for Figure 6.1, but here with 800-MHz/500-MHz ratios of bandwidths and corresponding standard deviations.

approximate vertical resolution of both setups (0.42 m, respectively 0.26 m) furthermore allows to separate between upper and lower edge of reflection bands (minimum bandwidth is 0.49 m). We can therefore conclude that the detected zones of high reflectivity represent real features of the subsurface. Same is true for the roughness of the horizons, represented by the standard deviation of depth-values. The roughness of internal reflection horizons, the spatial variability in depth, will be discussed in the following.

6.2. Local-scale spatial variability in snow accumulation

The internal reflection horizons were investigated in respect to the surface at reference-level. Consequently one has to distinguish between observed patterns of the sub-surface, and mirrored pattern of the surface topography. A wave-like surface could explain the wave-like appearance of internal reflection horizons. Larger reflection depths would be obtained, when the radar antennae are positioned on a crest,

6.2. Local-scale spatial variability in snow accumulation

and a smaller ones, when located in a through. There are indeed some indications in the surface-elevation model (Figure 5.2) that this is actually the case.

No systematic dipping of internal horizons can be observed over the area of the grid. Since normal distribution of depth-values can be assumed, one standard deviation (the depth-range from the horizon containing 68.3 % of the data) serves as first order approximation of the local-scale spatial variability in snow accumulation. The standard deviation is therefore a measure of the representativeness of layer depths from point measurements within that area. Table 6.1 lists mean traveltime, depth and corresponding standard deviations of the bands' centerlines, as well as the associated mean bandwidths. For comparison, results from lines derived by the single-line picking-method are also given. Applying the single-line method it was

Table 6.1.: Comparison of internal reflection horizons with respect to depth and spatial variability. Results are given for horizons digitized by the single line method (sl) and for computed band centerlines (c) taking into account both 500 and 800 MHz measurements.

IRH	Traveltime \bar{t} [ns]	Depth $\bar{d} \pm 1 \text{ S.D.}$ [m]	Band width $\bar{b} \pm 1 \text{ S.D.}$ [m]	Velocity* \bar{v} [m ns ⁻¹]
IRH-15 sl	15.3	1.82 \pm 0.12		
IRH-15 c	15.5	1.84 \pm 0.12	0.49 \pm 0.13	0.237
IRH-25 sl	24.0	2.74 \pm 0.18		
IRH-25 c	24.2	2.76 \pm 0.16	0.73 \pm 0.21	0.228
IRH-35 sl	35.7	3.96 \pm 0.22		
IRH-35 c	35.9	3.99 \pm 0.15	0.87 \pm 0.25	0.221
IRH-50 sl	52.0	5.66 \pm 0.20		
IRH-50 c	52.2	5.69 \pm 0.18	0.75 \pm 0.31	0.218
IRH-70 sl	70.4	7.59 \pm 0.20		
IRH-70 c	70.5	7.60 \pm 0.16	0.83 \pm 0.23	0.215
IRH-95 sl	97.3	10.36 \pm 0.18		
IRH-95 c	97.4	10.36 \pm 0.15	0.76 \pm 0.22	0.212

* Mean velocity between surface and depth of centerline, used to convert traveltime to width of associated band

tried to strictly follow maximum amplitudes, lying approximately in the center of the band. For the band-method, upper and lower edges were defined with a greater degree of horizontal generalization. Mean depth values for both picking approaches are similar, on average only 0.4 % smaller for results based on the single-line method,

6. Discussion & Conclusions

but produce larger standard deviations with values in the range from 0.12 to 0.22 m and an average of 0.18 m, against 0.11 to 0.18 m and a mean of 0.15 m for the centerlines. However, standard deviations for both methods are of the same order of magnitude. The absolute value of the standard deviation does not seem to change systematically with depth (in contrast to horizons along the 1 km sections, as we shall see later). They are of same order of magnitude for all horizons. Continuous gradients in the accumulation pattern lead to higher standard deviations in the depths of older layers, compared to younger ones, although they may describe the same variability. To resolve this problem Richardson-Näslund and Holmlund (1999) expressed standard deviations in percentages, normalized by the mean depth of the particular layer. The absence of cumulative spatial variability effects over the area of the grid suggests, that the local-scale variability in snow accumulation at T05 is a rather random process. The topography of internal reflection horizons is controlled by the pattern of the buried sastrugi field of the particular year. Almost constant absolute standard deviations suggest that characteristic dimensions of sastrugi are not subject of large inter-annual variability. Exact position and shape of single sastrugis are, however, random.

Consequently, relative deviations of point measurements from the local mean is largest for most shallow layers and decrease for older layers, buried deeper. Around T05, results from snow pits or firn cores are likely to over- or underestimate layer depth by around 15 cm (1 S.D.), but might reach up to 30 cm in extreme cases (2 S.D.: range containing 95.4 % of the data). This corresponds to a relative over- or underestimation in depth, and hence accumulation of about 8 to 15 % (1 to 2 S.D.) for IRH-15, thought of as the last summer layer, but only 3 to 5% for IRH-50. The average standard deviation in relative terms for all six layers is about 4 %, both for the center- and single lines.

To point out relative variations over the grid, the contour-plots of IRH-15 and IRH-50 (Figure 5.4) are shown again in Figure 6.3, but here with layer depth, normalized by the mean depth, as mentioned above. Since contour-plots are based on an interpolation of weighted mean values at 121 grid-points, they only produce a lower limit of actual spatial variations. The range of variability corresponds well to the standard deviation reported in section 5.3—about ± 8 % for IRH-15, ± 3 % for IRH-50, respectively.

6.3. Large-scale spatial distribution of snow

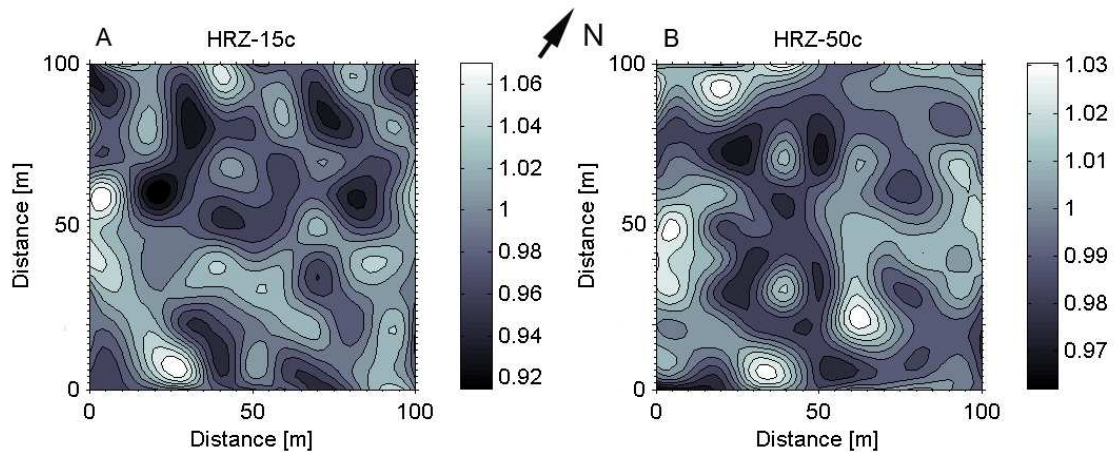


Figure 6.3.: Contour plots of normalized depths of selected internal reflection horizons (centerline). Last summer's percolation layer (A) and horizon around 50 ns traveltime (B). Note the direction of North.

6.3. Large-scale spatial distribution of snow

The obvious dipping of internal horizons over the area of the 1 x 1 km² square was reported in section 5.3. Statistical analysis of IRH depths, reveal a clear trend of increasing standard deviation with depth. To further investigate the gradient, selected 800-MHz sections oriented parallel or perpendicular to the slope were analyzed. IRH-centerlines are very well represented by their fitted linear approximation. Depth values seem to be randomly distributed around the regression lines (Figure 6.4). Panel (A) shows the down-slope section, perpendicular to the slope, stretching from point T05 south-eastwards. The horizons appear to be parallel to the surface. The same is true for the parallel section 1-km up-slope, displayed in panel (B), but horizons lie significantly deeper. More than half a meter in case of the deepest horizon. The section parallel to the slope, following the EGIG-line from T05 east-north-eastwards (C), reveals horizons which are clearly dipping towards north-east. Also here, the trend is well represented by the linear approximation, indicating that the gradient in snow accumulation is linear. In order to analyze if the dipping is a cumulative result of a constant spatial gradient in snow accumulation, or rather caused by a certain period of unusual snow distribution, unit thicknesses enclosed by adjacent horizons were computed, numbered 1 to 6. Units were then normalized by their corresponding mean thickness. The fitted linear regression lines pass through the centroid (x-mean, y-mean). A positive gradient in snow accumula-

6. Discussion & Conclusions

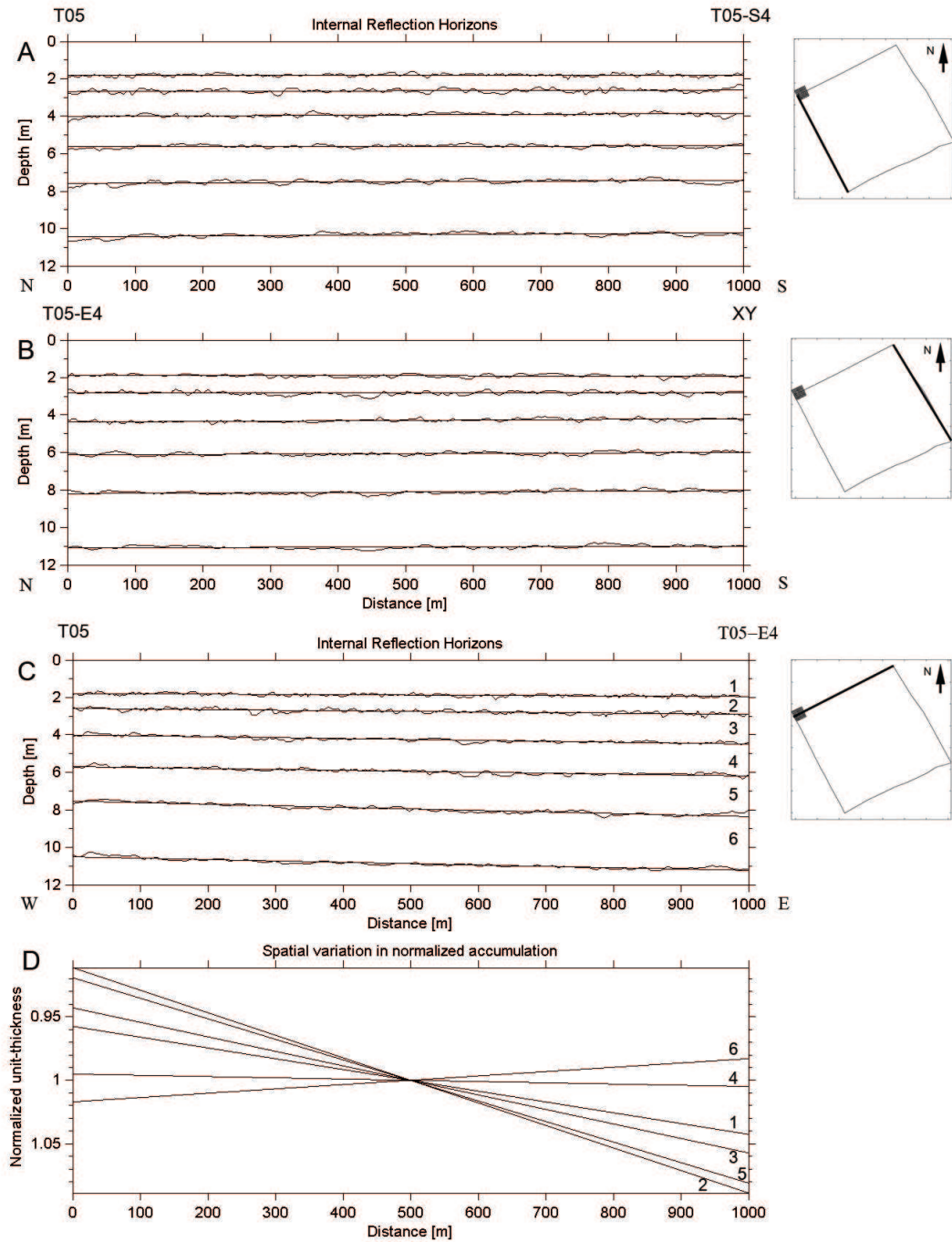


Figure 6.4.: Spatial variation in accumulation along 1-km sections. (A) and (B) show sections extending perpendicular and (C) parallel to the slope. Positions of the centerlines, and corresponding linear regression line are plotted. (D) displays the normalized accumulation for periods enclosed by adjacent horizons in (C), with profile-center crossing the mean ($\hat{=}$ 1).

tion towards the northeast persists for most of the periods in which units had been accumulated. Layer thicknesses increase by about 10 % from southwest to northeast (units 1,2,3 and 5). It is reversed for the deepest unit 6. Here, the unit thickness is about 3 % greater at the eastern, than at the western end. The thickness of unit 4 is almost constant.

6.4. Radar measurements versus firn-core records

GPR images arise from convolution of the input radar with the sub-surface. In order to evaluate the radar measurements and to test the travelttime-depth conversion I compare a density-based permittivity profile with traveltimes of major reflection horizons in the GPR section (Figure 6.5). With the assumption of negligible effects of liquid water content, the conversion to depth was reduced to a relation based on measured bulk density. The well known velocities of electromagnetic waves in air and pure ice serve as upper and lower limit of the travelttime-depth conversion. The density data was also used to derive snow permittivity via equation 2.17. The 5 m wide stripe of GPR data is centered at T05-E3, the borehole location of the core. Grey shaded stripes in the center plot represent average locations of reflection bands at T05-E3, determined by inverse distance weighting of all nearby sections (search radius of 3.5 m). Averaged reflection bands correlate very well with strong reflections in the selected 500 MHz GPR section, but appear deeper, than possible associated peaks in the permittivity profile. Intersections of lines drawn from significant permittivity peaks ($\epsilon' \gtrsim 2.5$) and the upper edge of reflection bands, marked with a “x” lie, however, close to the line representing the travelttime-depth relation. The choice of permittivity peaks is not unambiguous. Intersecting lines are also drawn for two reflections visible in the radargram, but not tracked. Misfits in the correlation can partly be explained by the fact, that GPR integrates returns over a certain area, while the firn core represents a point measurement. The irregular resolution of the core is furthermore very coarse, up to ≈ 15 cm.

Combined studies of physical snow properties and ground-penetrating radar measurements associated the very intense scattering of radar signals in the percolation facies of the Greenland Ice Sheet with massive zones of ice layers (e.g. Zabel *et al.*

6. Discussion & Conclusions

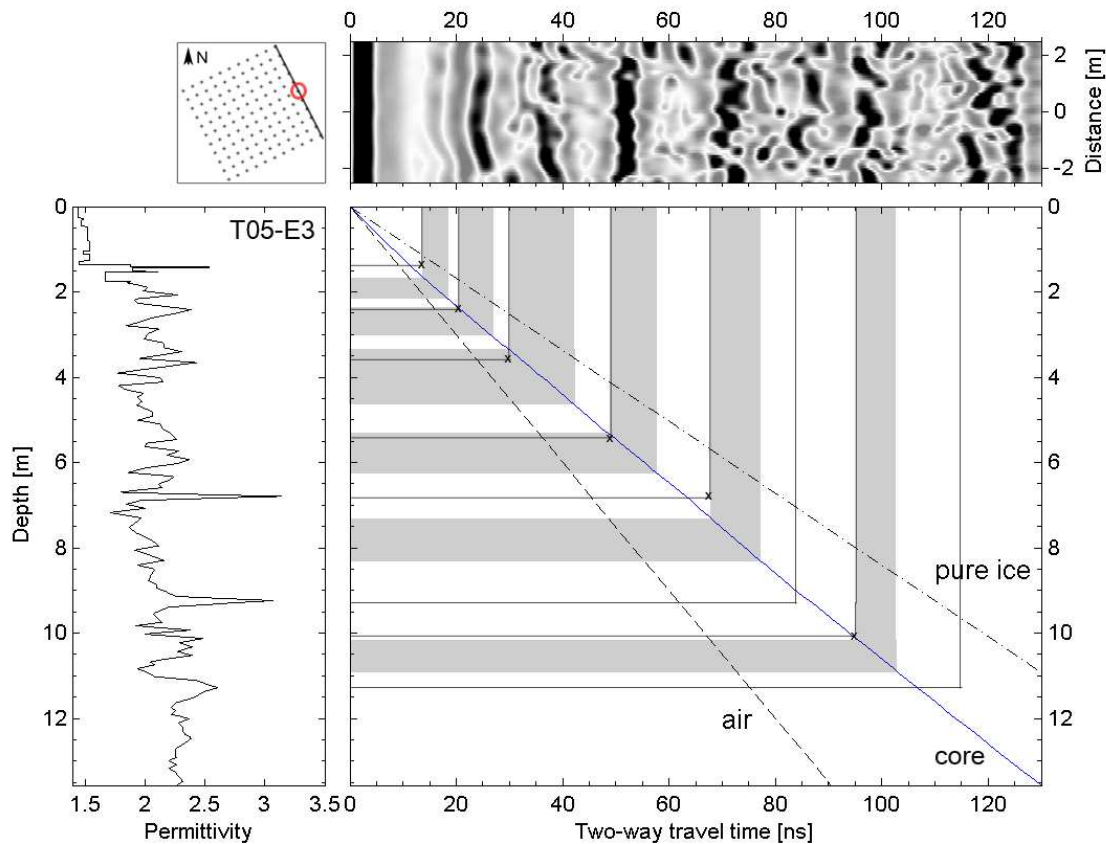


Figure 6.5.: Correlation between GPR data and firn-core record. The 5 m wide stripe of 500 MHz GPR profile is centered at the borehole of the core.

(1995); Jezek *et al.* (1994); Rignot *et al.* (1993). Individual zones were reported to reach a thickness of up to about 1 m.

In the percolation zone summer melting at (or close to) the surface causes the penetration of meltwater into the previous winter's snow pack. Temperatures of the snow pack are generally below freezing point, so that the distribution of meltwater is spatially restricted to active channels, along which the meltwater can percolate downwards. Buried wind or radiation crusts form interfaces that act as barriers which cause meltwater to pond locally and spread out laterally. These layers are characterized by their reduced hydraulic conductivity. However, they are not completely impermeable and allow limited flow through pores, as well as larger drains (pipes) leading through them. The introduction of water causes rapid metamorphism of snow and large crystals grow on the expense of smaller ones (Colbeck *et al.*, 1980). When refrozen, this features form a network of ice layers, lenses and

pipes embedded in a matrix of coarse-grained snow crystals. Ice layers and lenses are typically a few millimeters to centimeters thick and extend over several decimeters. Ice pipes, relics of the vertical channels feeding the horizontal ice structures, may be 10-20 cm wide and 10 to 100 cm long (Jezek *et al.*, 1994). Rignot *et al.* (1993) reports that it is the uppermost massive ice-layer zone, from where the major contribution to the total backscattered signal originates.

It is very likely, that massive ice-layer zones are also the source of reflections in the present radar data. Accordingly, the centreline of each band can be interpreted as an average position of an ice-layer zone, but the upper edge of each band should be a better estimate for the isochron, known as the last summer surface. The last summer surface, generally utilized for calculating mass-balance rates, is often clearly visible in the snow stratigraphy as a continuous ice layer. The GPR, however, can not separate this individual layer from adjoining ice structures below.

6.5. Accumulation rate estimates

Cumulative mass, divided by the corresponding time of accumulation yields accumulation rate. For this study, no age estimates for the horizons are available. However, the age can be approximated by dividing the cumulative mass above a particular horizon by the mean accumulation rate at the site, reported from earlier studies. Fischer *et al.* (1995) derived accumulation rates along the EGIG-line based on isotopic and chemical analysis of firn cores covering the upper 15 m of the pack. For a period corresponding to approximately 15 to 20 years of snow accumulation they found an annual mean of $460 \pm 102 \text{ kg m}^{-3}$ at T05. Utilizing these age estimates, the accumulation rate can be computed based on the radar investigation (table 6.2). The values should be treated with caution, since no independent dating is available.

However, mean accumulation rates calculated by dividing cumulative-mass values by the estimated number of years give reasonable results ranging from 428 to $485 \text{ kg m}^{-2}a^{-1}$. The age estimates are furthermore in agreement with the visible interpretation of the radargrams. Theoretically missing summer layers fit the order of identifiable but poorly visible internal reflection horizons. Variations are larger, if the mean accumulation rate is calculated for adjacent horizons. Remarkably is the maximum value of $598 \text{ kg m}^{-2}a^{-1}$ for the period from summer 2001 to sum-

6. Discussion & Conclusions

Table 6.2.: Corresponding depth, cumulative mass and estimate of age and annual mean accumulation for digitized horizons

IRH	Depth* (m)	Cumulative mass* (kg m ⁻²)	Accumu- lation# time	Age estimate	Mean acc. rate [§] (kg m ⁻² a ⁻¹) to top period	
Top	0	0	0	2004	–	–
IRH-15	1.61	473	1.03	2003	473	473
IRH-25	2.42	856	1.86	2002	428	383
IRH-35	3.58	1454	3.16	2001	485	598
IRH-50	5.34	2338	5.08	1999	468	442
IRH-70	7.19	3332	7.24	1997	476	497
IRH-95	10.22	4830	10.50	1994	483	499

* values correspond to upper edge of digitized bands including both 500 and 800-MHz results

cumulative mass divided by mean accumulation rate of 460 kg m⁻²a⁻¹, (Fischer *et al.*, 1995)

§ for period enclosed by surface and horizon (to top) and consecutive horizons (spec. period)

mer 2002 and the minimum value of 383 kg m⁻²a⁻¹ from 2002 to 2003. A possible explanation is the record summer melt all over the Arctic, during the year 2002, leading to a significant enlargement of the Greenland Ice Sheet’s melt zone (reference!!!). In autumn, at times where the winter snow pack usually starts to develop, a prolonged and extreme summer season could have caused continuous surface melt or precipitation in form of rain. The upper edge of this particular reflection band could therefore be interpreted rather as an autumn than a summer isochron, explaining the large deviation from the mean for that two periods. In average these two effects balance out. The mean accumulation rate for the period 2001 to 2003 yields 491 kg m⁻²a⁻¹. Other features visible in the radar data might be related as well to the record summer of 2002. The widest band (0.87 m) was observed for the percolation layer associated with the summer 2001 (IRH-35). It is likely, that the the high summer temperatures and extensive surface melt in 2002 were sufficient to raise the temperature of the gross if not all of the previous winter’s snowpack to pressure melting point. Conditions comparable to those of the wet snow or soaked zone might have allowed percolation of meltwater through the complete pack, before it refroze on top of the summer surface of 2001. Due to the integral effect of the backscattered radar signal, this ice layer might not be separable from the underlying

ice-layer zone of 2001, and hence yielding the maximal observed width. It is also this layer, for which the maximum difference in frequency-dependent relative layer depth occurs (Figure ??). An indication, that these features might be separable with the 800-MHz, but not with the 500-MHz system. Saturation of almost the whole 2001/02 winter snowpack is also indicated by the very complex and intense backscatter from the corresponding depth interval ($\sim 2.5\text{-}4$ m).

This interpretation, if true, implicates that GPR measurements, comparable to the one of the present study, could be utilized to identify and investigate recent extreme summer events, either by analyzing the widths of high reflectivity zones, related to the thickness' of annual ice-layer zones, or by mapping possible extension of the percolation zone into the dry-snow zone. Ice-layer zones, characteristic for the percolation zone remain preserved, buried under progressive snow accumulation. The depth range, and hence the timewindow from which such information could be achieved from, is, however, limited by the balance between penetration depth and resolution.

or better like this?

This interpretation, if true, implicates that GPR measurements, comparable to the one of the present study, could be utilized to identify and investigate recent extreme summer events, for example by analyzing widths of high reflectivity zones, related to the thickness' of annual ice-layer zones, and thereby mapping possible extension of the wet-snow zone. The saturation of the wet-snow zone allows distribution of meltwater over a larger scale. An important fact, contributing possible net-mass losses during that particular year. The depth range, and hence the timewindow from which such information could be achieved from, is, however, limited by the balance between penetration depth and resolution.

Bibliography

- Arendt, A., Echelmeyer, K., Harrison, W., Lingle, C., and Valentine, V., 2002. Rapid wastage of Alaska glaciers and their contribution to rising sea level. *Science*, 297, 382–386.
- Baldwin, D. J., Bamber, J. L., Payne, A. J., and Layberry, R. L., 2003. Using internal layers from the Greenland Ice Sheet, identified from radio echo sounding data, with numerical models. *Annals of Glaciology*, 37, 325–330.
- Bamber, J., Krabill, W., Raper, V., and Dowdeswell, J., 2004. Anomalous recent growth of part of a large Arctic ice cap: Austfonna, Svalbard. *Geophysical Research Letters*, 31, L12402–1 – L12402–4.
- Benson, C., 1962. Stratigraphic studies in the snow and firn of the Greenland Ice Sheet. CRREL Research Report, 70.
- Bindschadler, R., 1984. Jacobshavn glacier drainage basin: a balance assesment. *Journal of Geophysical Research*, 89, 2066–72.
- Björnson, H., Gjessing, Y., Hamran, S., Hagen, J., Liestøl, O., Pálson, F., and Erlingson, B., 1996. The thermal regime of sub-polar glaciers mapped by multi-frequency radio-echo sounding. *Journal of Glaciology*, 42, 23–32.
- Bogorodsky, V., Bentley, C., and Gudmansen, P., 1985. Radioglaciology. D. Reidel Publishing Company, Dordrecht, Holland.
- Colbeck, S., Male, D., Ashton, G., Hibler, W., Paterson, W., Perla, R., Raymond, C., and Robe, R., 1980. Dynamics of Snow and Ice Masses. Academic Press.

- CryoSat Science Advisory Group, 2001. CryoSat Calibration & Validation Concept. Technical report, Centre for Polar Observation & Modelling, Dept. of Space & Climate Physics, University College London, London, U.K.
- Dowdeswell, J. and Evans, S., 2004. Investigations of the form and flow of ice sheets and glaciers using radio-echo sounding. *Reports on Progress in Physics*, 67, 1821–1861.
- Eisen, O., 2003. On the nature, interpretation, and application of electromagnetic reflections in cold ice, volume 474 of *Reports on Polar and Marine Research*. Alfred Wegener Institute for Polar and Marine Research, Bremerhaven.
- Eisen, O., Nixdorf, U., Wilhelms, F., and Miller, H., 2002. Electromagnetic wave speed in polar ice: validation of the common-midpoint technique with high resolution dielectric-profiling and γ -density measurements. *Annals of Glaciology*, 34, 150–156.
- Eisen, O., Nixdorf, U., Wilhelms, F., and Miller, H., 2004. Age estimates of isochronous reflection horizons by combining ice core, survey, and synthetic radar data. *Journal of Geophysical Research*, 109(B4), B4106–1 – B04106–11.
- Evans, S., 1963. Radio techniques for the measurement of ice thickness. *The Polar Record*, 11(75), 406–411.
- Fischer, H., Wagenbach, D., Latenser, M., and Haeberli, W., 1995. Glaciometeorological and isotopic studies along the EGIG line, central Greenland. *Journal of Glaciology*, 41(139), 515–527.
- Fujita, S. and Mae, S., 1994. Causes and nature of ice-sheet radio-echo internal reflections estimated from the dielectric properties of ice. *Annals of Glaciology*, 20, 80–86.
- Glen, J. and Paren, J., 1975. The electrical properties of snow and ice. *Journal of Geophysical Research*, 15(73), 15–38.
- Hempel, L., 1994. Der Zentralteil des grönländischen Inlandeises: Ergebnisse aus hochauflösenden elektromagnetischen Reflektionsmessungen. PhD thesis, Westfälische Wilhelms-Universität Münster.

Bibliography

- Hubbard, B. and Glasser, N., 2005. *Field Techniques in Glaciology and Glacial Geomorphology*. John Wiley & Sons, Ltd, London, UK.
- Jacobel, R. and Hodge, S., 1995. Radar internal layers from the Greenland summit. *Geophysical Research Letters*, 22(5), 587–590.
- Jezek, K., Gogineni, P., and Shanableh, M., 1994. Radar Measurements of Melt Zones on the Greenland Ice Sheet. *Geophysical Research Letters*, 21(1), 33–36.
- Kanagaratnam, P., Gogineni, S. P., Gundestrup, N., and Larsen, L., 2001. High Resolution radar mapping of internal layers at the North Greenland Ice Core Project. *Journal of Geophysical Research*, 106(D24), 33,799–33,811.
- Kohler, J., Moore, J., Kennett, M., Engeset, R., and Elvehøy, H., 1997. Using ground-penetrating radar to image previous years' summer surfaces for mass-balance measurements. *Annals of Glaciology*, 24, 355–360.
- Kovacs, A., Gow, A., and Morey, R., 1995. The in-situ dielectric constant of polar firn revisited. *Cold Regions Science and Technology*, 23, 245–256.
- Krabill, W., Abdalati, W., Fredericks, E., Manizade, S., Martin, C., Swift, R., Thomas, R., Wright, W., and Yungel, J., 2000. Greenland Ice Sheet: high-elevation balance and periperal thinning. *Science*, 289, 428–430.
- Létréguilly, A., Reeh, N., and Huybrechts, P., 1991. The Greenland ice sheet through the last glacial-interglacial cycle. *Paleogeography, Palaeoclimatology, Palaeoecology*, 90, 385–394.
- Looyenga, H., 1965. Dielectric constant of heterogeneous mixtures. *Physica*, 31(3), 401–406.
- Mari, J., Glangeaud, F., and Coppens, F., 1999. *Signal Processing for Geologists and Geophysicists*. Edition Technip.
- Oswald, G., 1975. Investigation of sub-ice bedrock characteristics by radio-echo sounding. *Journal of Glaciology*, 15, 75–87.
- Oswald, G. and Robin, G. d. Q., 1973. Lakes Beneath the Antarctic Ice Sheet. *Nature*, 245(5423), 251–254.

- Paradigm Geophysics, 1995. DISCO User's Manual. CogniSeis Development.
- Paterson, W., 1994. *The Physics of Glaciers*. Elsevier Science Ltd, Oxford, UK, third edition.
- Petrenko, V. and Whitworth, R., 1999. *Physics of Ice*. Oxford University Press, Oxford, UK.
- Petterson, R., Jansson, P., and Holmlund, P., 2003. Cold surface layer thinning on Storglaciären, Sweden, observed by repeated ground penetrating radar surveys. *Journal of Geophysical Research*, 108(F1), 5.1–5.9.
- Richardson, C., Aarholt, E., Hamram, S.-E., Holmlund, P., and Isaksson, E., 1997. Spatial distribution of snow in western Dronning Maud Land, East Antarctica, mapped by a ground-based snow radar. *Journal of Geophysical Research*, 102(B9), 20,343–20,353.
- Richardson-Näslund, C., 2001. Spatial distribution of snow in Antarctica and other glacier studies using ground-penetrating radar. PhD thesis, The Department of Physical Geography and Quaternary Geology, Stockholm University.
- Richardson-Näslund, C. and Holmlund, P., 1999. Spatial variability in shallow snow-layer depths in central Dronning Maud Land, East Antarctica. *Annals of Glaciology*, 29, 10–16.
- Rignot, E., Ostro, S., van Zyl, J., and Jezek, K., 1993. Unusual Radar Echoes from the Greenland Ice Sheet. *Science*, 261, 1710–1713.
- Robin, G., 1975. Velocity of radio waves in ice by means of a bore-hole interferometric technique. *Journal of Glaciology*, 15(73), 151–159.
- Siegert, M., Dowdeswell, J., Gorman, M., and McIntyre, N., 1996. An inventory of Antarctic sub-glacial lakes. *Antarctic Science*, 8(3), 281–286.
- Sinisalo, A., Grinsted, A., Moore, J., Kärkäs, E., and Petterson, R., 2003. Snow-accumulation studies in Antarctica with ground-penetrating radar using 50, 100 and 800 MHz antenna frequencies. *Annals of Glaciology*, 37, 194–198.

Bibliography

- Steinhage, D., 2001. Contributions of geophysical measurements in Dronning Maud Land, Antarctica, locating an optimal drill site for a deep ice core drilling, volume 384 of Reports on Polar and Marine Research. Alfred Wegener Institute for Polar and Marine Research, Bremerhaven.
- Telford, W., Geldart, L., and Sheriff, R., 1990. Applied Geophysics. Cambridge University Press, 2 edition.
- Tiuri, M., Sihvola, A., Nyfors, E., and Hallikainen, M., 1984. The complex dielectric constant of snow at microwave frequencies. *Journal of Oceanographic Engineering*, OE-9(5), 377–382.
- Waite, A. and Schmidt, S., 1961. Cross errors in height indication from pulsed radar altimeters operating over thick ice or snow. In: Institute of Radio Engineers International Convention Record, volume 5, pp. 38–53.
- Walford, M., 1964. Radio echo sounding through an ice shelf. *Nature*, 204, 317–319.
- Walford, M., Kennett, M., and Holmlund, P., 1986. Interpretation of radio echoes from Storglaciren, Northern Sweden. *Journal of Glaciology*, 32(110), 39–49.
- Wolff, E., 2000. Electrical stratigraphy of polar ice cores: principles, methods, and findings. In: Hondoh, T. (Ed.), *Physics of Ice Core Records*. International Symposium on Physics of Ice Core Records, 14–17 September 1998, Shikotsukohan, Japan, pp. 155–184, Kita 9, Nishi 8, Kita-ku, Sapporo 060-0809, Japan. Hokkaido University Press.
- Xia, J., Franseen, E., Miller, R., and Weis, T., 2004. Application of deterministic deconvolution of ground-penetrating radar data in a study of carbonate strata. *Journal of Applied Geophysics*, 56, 213–229.
- Zabel, I., Jezek, K., and Baggeroer, P., 1995. Ground-based radar observations of snow stratigraphy and melt processes in the percolation facies of the Greenland ice sheet. *Annals of Glaciology*, 21, 40–44.

Acknowledgements

Kiitos!

A. Scripts & routines

```
*JOB   arkr04 041403 TDUNSE segy
**
** automatically created by
** /hs/userf/projects/arkr04/einrichten/dsk2segy.bat implementing
** /hs/userf/projects/arkr04/einrichten/gprdb2dsk_vT.sh
** a modified version of gprdb2dsk.sh by O.Eisen
** required options: -ws -phc -pf -pa -pt -f -b arkr04 041403
**
** LGC samprate    0.12621
** LGC time        0 129.236969
** LGC currline    AWI041403
** LGC traces      1033
**
*CALL   DSKRD    ../data-raw-dsk/041403.dsk
ENSMBLE SHOT
**
*CALL   HEADPUT CDP    STORE    INTEGER
INPUT  SHOT    INTERP DATA    1 1 DATA    1033    1033
**
*CALL   HEADPUT FARVL          FLOAT
INPUT  SHOT    NOINTERP
DATA   1       6.22    5.96    6.09    6.22    6.22\\
DATA   6       6.22    6.09    6.09    6.09    6.09\\
DATA   11      6.09    6.09    6.30    6.22    6.22\\
...\\
DATA   1021    6.22    6.22    6.22    6.22    6.09\\
DATA   1026    6.09    6.22    6.09    6.09    6.09\\
DATA   1031    6.30    6.56    6.43    0.00    0.00\\
**
*CALL   HDRMATH
HCMUL  FARVL  -1      FARVL    HCADD   FARVL   0.6     FARVL
**
*CALL   STATICH FARVL    APPLY
**
*CALL   FILTER  SHOT
KEYDEF 1 BAND          41
          350    430    680    820
**
*CALL   RUNMIX  5      MEAN
```

```
WEIGHTS 0.1    0.2    0.4    0.2    0.1
**
*CALL  ENVELOPE ENVELOP
**
*CALL  FILTER
KEYDEF 1      BUTTER 81
          30          250
**
*CALL  RUNMIX 5      MEAN
**
*CALL  AGC 20 1
**
*CALL  SORT 50    50
MAJOR  CDP  MINOR SHOT
**
*CALL  PRINT
SUMMARY MIN    AVG
**
*CALL  GOUT  SEGY      CDP
LIST DENSITY 6250 TAPEOPT /tapefile="/awi8/data/sy041403.tod"
**
*END
```

B. Data

B.1. GPR

B.2. GPS

B.3. Snow-stratigraphy

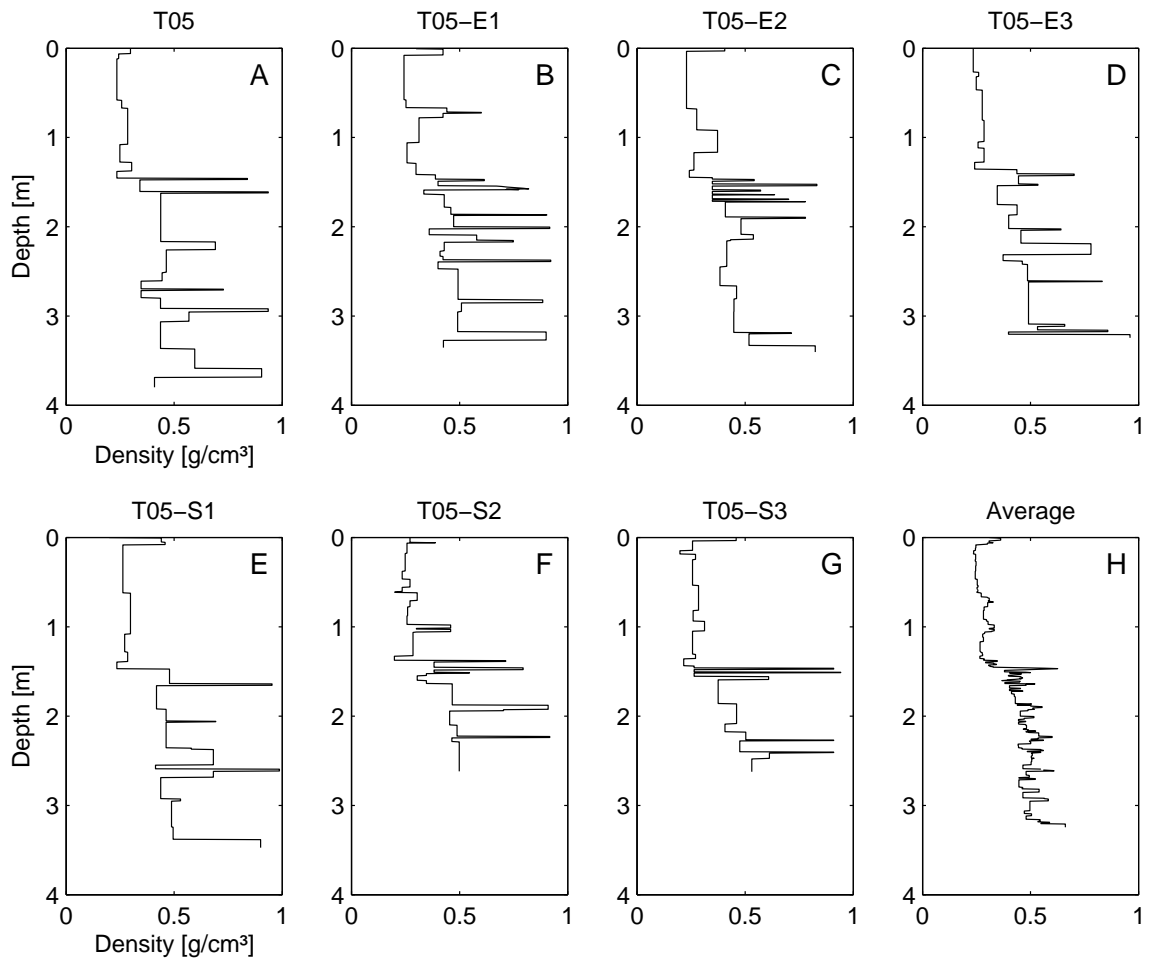


Figure B.1.: Density-depth profiles from snow-pits and shallow firn-cores (A-G) and resulting average (H).

C. Results

C.1. 100 by 100-m grid

C.1. 100 by 100-m grid

Table C.1.: Mean values of two-way traveltime (grid) for all horizons and picking methods

IRH	Type	Two-way traveltime [ns]					
		500 MHz	STD	800 MHz	STD	500 & 800 MHz	STD
15 ns	sl	15.3	1.1	15.3	1.0	15.3	1.1
	c	15.5	1.0	15.5	1.0	15.5	1.0
	u	13.6	1.0	13.2	0.9	13.4	0.9
	l	17.3	1.3	17.8	1.3	17.5	1.3
	b	3.7	1.0	4.5	1.1	4.1	1.1
25 ns	sl	23.8	1.7	24.1	1.8	23.9	1.8
	c	24.0	1.4	24.4	1.5	24.2	1.5
	u	21.0	1.4	21.0	1.6	21.0	1.5
	l	27.0	1.8	27.7	1.9	27.3	1.9
	b	6.0	1.8	6.7	1.9	6.4	1.9
35 ns	sl	34.7	2.1	36.9	2.1	35.7	2.1
	c	34.8	1.5	37.2	1.3	36.0	1.4
	u	31.1	1.8	33.1	1.7	32.0	1.7
	l	38.5	2.0	41.4	1.9	39.9	1.9
	b	7.4	2.2	8.3	2.3	7.9	2.2
50 ns	sl	51.1	1.9	52.9	1.3	52.0	1.6
	c	51.2	1.4	53.4	1.2	52.2	1.3
	u	47.4	1.5	50.2	2.0	48.7	1.7
	l	55.0	1.9	56.5	2.3	55.7	2.1
	b	7.6	2.1	7.0	1.8	7.3	2.0
70 ns	sl	69.0	1.9	72.0	1.8	70.4	1.9
	c	69.0	1.6	72.2	1.5	70.5	1.5
	u	65.1	1.8	68.3	1.7	66.7	1.7
	l	72.9	2.1	76.1	1.9	74.4	2.0
	b	7.7	2.2	7.7	2.1	7.7	2.2
95 ns	sl	94.8	1.8	100.1	1.7	97.3	1.8
	c	94.7	1.5	100.4	1.5	97.4	1.5
	u	91.2	1.7	96.6	1.7	93.8	1.7
	l	98.1	2.0	100.4	1.9	100.9	1.9
	b	6.9	2.0	7.5	2.1	7.2	2.0

C. Results

Table C.2.: Mean values of depth (grid) for all horizons and picking methods

IRH	Type	Depth/ Width [m]					
		500 MHz	STD	800 MHz	STD	500 & 800 MHz	STD
15 ns	sl	1.82	0.13	1.82	0.11	1.82	0.12
	c	1.84	0.11	1.84	0.10	1.84	0.11
	u	1.64	0.11	1.59	0.10	1.61	0.10
	l	2.03	0.14	2.08	0.14	2.06	0.14
	b	0.44	0.12	0.54	0.14	0.49	0.13
25 ns	sl	2.71	0.18	2.76	0.19	2.74	0.19
	c	2.74	0.15	2.78	0.16	2.76	0.16
	u	2.42	0.16	2.42	0.17	2.42	0.17
	l	3.06	0.19	3.13	0.20	3.09	0.20
	b	0.69	0.21	0.77	0.22	0.73	0.21
35 ns	sl	3.85	0.22	4.08	0.22	3.96	0.22
	c	3.86	0.16	4.12	0.14	3.99	0.15
	u	3.48	0.18	3.68	0.17	3.58	0.17
	l	4.26	0.21	4.56	0.20	4.41	0.21
	b	0.82	0.24	0.92	0.25	0.87	0.25
50 ns	sl	5.57	0.19	5.75	0.13	5.66	0.20
	c	5.59	0.14	5.80	0.12	5.69	0.13
	u	5.20	0.15	5.48	0.21	5.34	0.24
	l	5.97	0.20	6.12	0.24	6.05	0.24
	b	0.83	0.23	0.76	0.20	0.80	0.21
70 ns	sl	7.43	0.21	7.76	0.19	7.59	0.20
	c	7.43	0.17	7.78	0.15	7.60	0.16
	u	7.01	0.19	7.36	0.19	7.19	0.19
	l	7.85	0.22	8.18	0.20	8.01	0.21
	b	0.83	0.24	0.83	0.23	0.83	0.23
95 ns	sl	10.10	0.18	10.62	0.17	10.36	0.18
	c	10.08	0.15	10.64	0.15	10.36	0.15
	u	9.72	0.18	10.27	0.17	10.23	0.17
	l	10.42	0.20	11.03	0.19	10.72	0.18
	b	0.74	0.21	0.79	0.22	0.76	0.22

Table C.3.: Mean values of cumulative mass (grid) for all horizons and picking methods

IRH	Type	Accumulated mass [kg m^{-3}]					
		500 MHz	STD	800 MHz	STD	500 & 800 MHz	STD
15 ns	sl	562	56	561	50	562	53
	c	571	51	572	47	571	49
	u	483	46	463	42	473	44
	l	663	67	687	67	675	67
25 ns	sl	1000	89	1021	92	1010	91
	c	1013	73	1031	78	1022	75
	u	856	81	856	84	856	82
	l	1172	99	1210	107	1191	103
35 ns	sl	1593	110	1705	106	1649	108
	c	1600	79	1725	68	1662	74
	u	1399	97	1508	90	1454	187
	l	1789	101	1934	96	1861	99
50 ns	sl	2466	107	2568	77	2517	92
	c	2474	77	2596	69	2535	73
	u	2258	84	2418	113	2338	99
	l	2692	109	2773	129	2733	119
70 ns	sl	3446	97	3599	96	3523	96
	c	3445	79	3608	77	3526	78
	u	3254	90	3412	84	3332	87
	l	3645	111	3814	101	3729	106
95 ns	sl	4882	109	5194	94	5039	101
	c	4870	93	5207	81	5038	87
	u	4670	95	4990	104	4830	100
	l	5078	114	5416	117	5247	115

C. Results

Table C.4.: Comparison of antenna frequencies. Besides two-way traveltime values for both frequencies, 800 MHz values are expressed normalized by 500 MHz values.

IRH	Type	Two-way traveltime [ns]				Ratio (800 over 500)	
		500 MHz	1 S.D.	800 MHz	1 S.D.	TWT	1 S.D.
15 ns	c	15.5	1.0	15.5	1.0	1.001	0.913
25 ns	c	24.0	1.4	24.4	1.5	1.015	1.057
35 ns	c	34.8	1.5	37.2	1.3	1.069	0.876
50 ns	c	51.2	1.4	53.4	1.2	1.042	0.854
70 ns	c	69.0	1.6	72.2	1.5	1.046	0.912
95 ns	c	94.7	1.5	100.4	1.5	1.060	0.968
Sum	c	289.2	8.5	303.0	7.9	1.048	0.930
15 ns	b	3.7	1.0	4.5	1.1	1.237	1.163
25 ns	b	6.0	1.8	6.7	1.9	1.116	1.038
35 ns	b	7.4	2.2	8.3	2.3	1.119	1.055
50 ns	b	7.6	2.1	7.0	1.8	0.921	0.882
70 ns	b	7.7	2.2	7.7	2.1	0.997	0.959
95 ns	b	6.9	2.0	7.5	2.1	1.076	1.045
Sum	b	39.4	11.3	41.7	11.4	1.060	1.009

C.1. 100 by 100-m grid

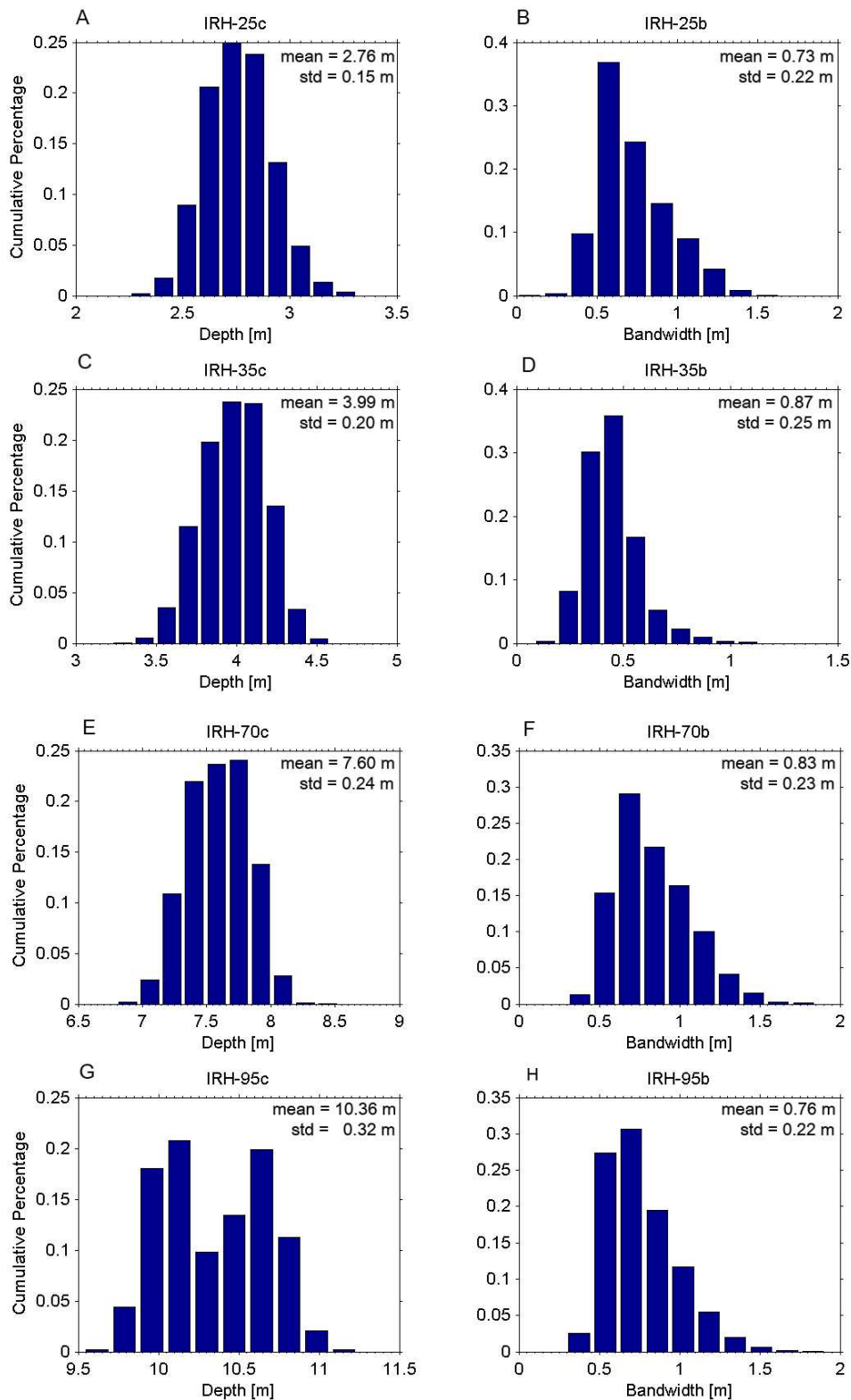


Figure C.1.: Histograms of IRH-depths and bandwidths for horizons around 25 ns traveltime (A and B), 35 ns traveltime (C and D), 70 ns traveltime (E and F) and 95 ns traveltime (G and H). Analyses based on 39715 samples.

C. Results

C.2. 1 by 1-km square

Table C.5.: Mean values of two-way traveltime (1 by 1-km square) for all horizons and picking methods

IRH	Type	Two-way traveltime [ns]					
		500 MHz	STD	800 MHz	STD	500 & 800 MHz	STD
15 ns	c	15.7	1.2	15.4	0.8	15.5	1.0
	u	13.8	1.2	13.3	0.7	13.6	0.9
	l	17.5	1.3	17.5	1.1	17.5	1.2
	b	3.7	0.6	4.2	0.8	3.9	0.7
25 ns	c	23.9	1.3	23.6	1.3	23.7	1.3
	u	21.4	1.2	21.3	1.3	21.3	1.2
	l	26.4	1.7	25.9	1.5	26.1	1.6
	b	5.0	1.1	4.6	0.9	4.8	1.0
35 ns	c	34.7	2.0	37.1	1.8	35.9	1.9
	u	31.6	1.9	33.4	1.9	32.5	1.9
	l	37.8	2.3	40.8	2.0	39.3	2.2
	b	6.3	1.1	7.5	1.2	6.9	1.1
50 ns	c	52.3	2.3	53.6	2.2	53.0	2.2
	u	48.9	2.2	50.8	2.1	49.9	2.1
	l	55.6	2.6	56.5	2.4	56.1	2.5
	b	6.7	1.3	5.7	1.0	6.2	1.1
70 ns	c	69.6	2.9	72.7	2.7	71.1	2.8
	u	66.5	2.9	69.4	2.7	67.9	2.8
	l	72.7	3.1	76.0	2.8	74.3	3.0
	b	6.2	1.3	6.6	1.3	6.4	1.3
95 ns	c	95.1	3.5	100.8	3.3	97.9	3.4
	u	92.0	3.3	97.4	3.3	94.7	3.3
	l	98.1	3.7	104.1	3.3	101.1	3.5
	b	6.1	1.1	6.7	1.0	6.4	1.0

C. Results

Table C.6.: Mean values of depth (1 by 1-km square) for all horizons and picking methods

IRH	Type	Depth/ Width [m]					
		500 MHz	STD	800 MHz	STD	500 & 800 MHz	STD
15 ns	c	1.86	0.13	1.83	0.09	1.84	0.11
	u	1.66	0.13	1.60	0.08	1.63	0.10
	l	2.05	0.14	2.06	0.11	2.05	0.13
	b	0.43	0.07	0.50	0.09	0.47	0.08
25 ns	c	2.73	0.14	2.70	0.14	2.71	0.14
	u	2.47	0.12	2.45	0.14	2.46	0.13
	l	2.99	0.18	2.94	0.16	2.97	0.17
	b	0.57	0.13	0.53	0.11	0.55	0.12
35 ns	c	3.85	0.21	4.10	0.20	3.98	0.20
	u	3.52	0.19	3.71	0.19	3.62	0.19
	l	4.18	0.25	4.50	0.22	4.34	0.23
	b	0.69	0.13	0.82	0.13	0.76	0.13
50 ns	c	5.69	0.23	5.83	0.22	5.76	0.23
	u	5.35	0.22	5.54	0.21	5.45	0.22
	l	6.03	0.26	6.12	0.24	6.08	0.25
	b	0.73	0.14	0.62	0.11	0.67	0.12
70 ns	c	7.49	0.32	7.82	0.29	7.66	0.30
	u	7.16	0.31	7.47	0.30	7.31	0.30
	l	7.82	0.33	8.17	0.30	8.00	0.31
	b	0.67	0.14	0.71	0.14	0.69	0.14
95 ns	c	10.11	0.35	10.69	0.33	10.40	0.34
	u	9.81	0.33	10.35	0.33	10.08	0.33
	l	10.42	0.38	11.03	0.33	10.72	0.35
	b	0.65	0.11	0.71	0.11	0.68	0.11

Table C.7.: Mean values of cumulative mass (1 by 1-km square) for all horizons and picking methods

IRH	Type	Accumulated mass [kg m^{-3}]					
		500 MHz	STD	800 MHz	STD	500 & 800 MHz	STD
15 ns	c	581	59	568	40	574	49
	u	493	55	468	34	480	44
	l	673	66	674	54	673	60
25 ns	c	1007	70	992	69	999	69
	u	878	62	871	68	875	65
	l	1137	91	1112	80	1124	85
35 ns	c	1592	107	1717	94	1654	101
	u	1424	106	1523	99	1474	103
	l	1752	116	1906	103	1829	109
50 ns	c	2536	132	2613	126	2574	129
	u	2344	124	2449	119	2397	121
	l	2724	145	2773	132	2749	139
70 ns	c	3476	147	3634	142	3555	145
	u	3316	148	3465	137	3391	142
	l	3635	163	3810	152	3722	157
95 ns	c	4900	206	5226	184	5063	195
	u	4722	185	5033	198	4877	191
	l	5073	218	5429	195	5251	206

C. Results

Table C.8.: Spatial variability in accumulation (1 by 1-km square). Mean centerline-depth for whole square and along 8 points, 500 m spaced, starting clockwise from T05 (1). Values are a linear weighted mean of data points falling in a circular area with 100 m radius.

IRH	Averaged layer depth [m]								
	All	1 (T05)	2	3 (T05-E4)	4	5 (XY)	6	7 (T05-S4)	8
15 c	1.84	1.81	1.92	1.94	1.94	1.91	1.81	1.77	1.73
25 c	2.71	2.64	2.80	2.87	2.84	2.81	2.65	2.57	2.61
35 c	3.98	3.86	4.11	4.26	4.11	4.11	3.87	3.77	3.74
50 c	5.76	5.65	5.89	6.04	5.97	5.92	5.71	5.49	5.45
70 c	7.66	7.47	7.85	8.01	7.99	7.88	7.59	7.30	7.25
95 c	10.4	10.19	10.58	10.81	10.74	10.71	10.29	9.97	9.89
Normalized layer depth									
15 c	1	0.981	1.042	1.056	1.056	1.036	0.985	0.961	0.941
25 c	1	0.974	1.033	1.059	1.048	1.036	0.978	0.947	0.961
35 c	1	0.969	1.034	1.070	1.033	1.032	0.973	0.946	0.940
50 c	1	0.981	1.022	1.049	1.037	1.027	0.991	0.954	0.946
70 c	1	0.976	1.025	1.046	1.043	1.028	0.991	0.954	0.947
95 c	1	0.980	1.018	1.040	1.032	1.029	0.989	0.959	0.951
Mean	1	0.977	1.029	1.053	1.042	1.031	0.984	0.953	0.948

D. Erklärung

gem. § 14 Abs. 5, bzw. § 8 Abs. 2 Nr. 2

PO Studiengang Geowissenschaften

Ich versichere hiermit, dass ich diese Diplomarbeit selbstständig verfasst und keine anderen als die angegebenen Quellen und Hilfsmittel verwendet habe.

Desweiteren erkläre ich, dass ich weder eine Diplomprüfung im Studiengang Geowissenschaften oder einem verwandten Studiengang nicht bestanden habe, noch befinde ich mich in einem Prüfungsverfahren.

Ich bin damit einverstanden, dass die Diplomarbeit in unveränderter Fassung der Öffentlichkeit zur Verfügung gestellt werden kann.

Bremen, den 29.05.2006

.....

Thorben Dunse